Preprint typeset in JHEP style - HYPER VERSION MPP-2014-109, ZU-TH 15/14, LPN14-064

arXiv:1404.5572v2 [hep-ph] 5 Sep 2014

Top-squark pair production at the LHC: a complete analysis at next-to-leading order

Jan Germer*

Max-Planck-Institut für Physik, Föhringer Ring 6, D-80805 München, Germany;
Email: germer@mpp.mpg.de

Wolfgang Hollik

Max-Planck-Institut für Physik, Föhringer Ring 6, D-80805 München, Germany;
Email: hollik@mpp.mpg.de

Jonas M. Lindert

Physik-Institut, Universität Zürich, Winthertur erstrasse 190, CH-8057 Zürich, Switzerland; E-mail: lindert@physik.uzh.ch

Edoardo Mirabella

Max-Planck-Institut für Physik, Föhringer Ring 6, D-80805 München, Germany;
E-mail: mirabell@mpp.mpg.de

Abstract: We present a complete next-to-leading order study of top-squark pair production at the LHC, including QCD and EW corrections. The calculation is performed within the Minimal Supersymmetric Standard Model and numerical results are presented for parameter regions compatible with the observed Higgs boson. We employ the most recent parton distribution functions including QED corrections and we find NLO EW corrections to the inclusive stop-pair production cross section up to $25 - 30\%$ compared to the leading-order prediction. Besides corrections to inclusive cross sections also important kinematic distributions are investigated.

*Now at PRÜFTECHNIK Condition Monitoring GmbH.

Contents

1. Introduction **1**

2. Computational details **3**

3. Numerical analysis **5**

3.1 Total cross section 6

3.2 Differential distributions 10

4. Conclusions **11**

1. Introduction

The discovery of a signal in the Higgs boson searches at the LHC [1, 2] has triggered extensive studies of the properties of this particle, in particular of its mass, couplings and spin [3, 4]. The experimental results are in agreement with Standard Model (SM) predictions. Nevertheless, experimental evidence for beyond the Standard Model (BSM) physics may still be found in the future run, in particular for the minimal supersymmetric extension of the Standard Model (MSSM), where the value of the Higgs boson mass can naturally be explained.

The MSSM is an appealing BSM scenario allowing for precise quantitative predictions which can be tested in the LHC experiments. To date, the searches at the LHC have investigated various final states and signatures [5, 6], without finding deviations from the SM, thus setting limits in several regions of the MSSM parameter space. Such searches are based on direct production of supersymmetric (SUSY) partners of the SM particles, in particular on processes producing strongly-interacting SUSY particles. The importance of these production channels is reflected in the extensive efforts spent in improving their theoretical predictions, including not only the leading-order (LO) contributions [7–11], but also the next-to-leading-order (NLO) QCD [12–16], the tree-level electroweak (EW) [17–24] and the $\mathcal{O}(\alpha_s^2\alpha)$ [19, 21, 24–28] corrections to the cross sections. The large radiative corrections in the threshold region have been resummed at the next-to-leading logarithmic (NLL) accuracy [29–33], and resummation of soft-gluon and Coulomb corrections has been performed within an effective field theory approach [34–37]. Resummations at the next-to-next-to-leading logarithmic (NNLL) accuracy have been performed as well [38–42]. Gluino [43] and stop [44] bound states as well as bound-state effects in gluino-gluino and squark-gluino production [45–47] have been studied. Approximate next-to-next-to-leading-order (NNLO) predictions for quark–anti-squark production are available [48–51]. The decay

rate of squarks is known at NLO, including both the QCD [52–54] and the EW corrections [55, 56]. The decay rate of the gluino in a quark-squark pair is known at NLO QCD as well [52, 54]. Furthermore, phenomenological studies have been performed including systematically NLO QCD corrections to the production and the subsequent decay of stop–anti-stop [57,58] and squark–squark pairs [59,60]. In the case of squark–squark production, the NLO QCD corrections have been matched with parton showers in Ref. [61].

Experimentally the production of third generation squarks is different from those of the other generations. Final-state bottom and top quarks from the decays of the squarks can be distinguished from their light-flavor counterparts. This leads to characteristic signatures which are extensively used in the experimental searches for SUSY at the LHC [62–67]. These searches assume a dominant decay channel and put limits on the mass of the light stop, $\tilde{t}_1$, and of the decay products. For instance the analysis in Ref. [67] puts a lower bound on the $\tilde{t}_1$ one, $m_{\tilde{t}_1} \geq 750$ GeV, assuming 100% branching ratio into a massless neutralino $\tilde{\chi}_1^0$.[1] In the experimental analyses signal events are usually produced at LO and the total cross section is normalized to NLO QCD + NLL accuracy using the codes `Prospino` [68] and `NLL-fast` [33], along the lines of Ref. [69]. The theoretical uncertainty on the generated signal is obtained by varying the parton distribution function (PDF) sets and the renormalization/factorization scale. For a hadronic center-of-mass energy $\sqrt{S} = 14$ TeV, the obtained uncertainty is depicted in Fig. 1. It is below 15% (20%) for masses below 1000 (1400) GeV. It is worth to mention that this procedure does not provide an accurate estimation of the impact of the higher order contributions. Indeed, the latter may depend strongly on the kinematics of the final state changing the shapes of differential distributions. Higher-order contributions to the decays of the produced particles can have substantial effects as well [57–60].

In this paper we analyze the numerical impact of the NLO EW corrections to the total cross section of the hadronic pair-production of the lightest top-squark $\tilde{t}_1$,

$$p\,p \to \tilde{t}_1\,\tilde{t}_1^*\,, \tag{1.1}$$

by presenting the first phenomenological study combining NLO QCD and NLO EW corrections. A similar study of the NLO EW corrections has already been published in [19]. There, results were presented for a handful of Snowmass points [70] and for benchmark slopes passing along the SPS1a′ scenario [71]. NLO EW corrections to inclusive cross sections were found to be small, below 5%, while differential distributions were found to be affected by up to 20% in their tails. In view of the developments over the recent years, updated and improved analyses are considered appropriate. Firstly, the previous study focuses purely on the EW corrections without including the (dominant) NLO QCD corrections. Only a consistent treatment of NLO QCD and NLO EW including common PDFs allows for a quantitative comparison. Secondly, in the MSSM the mass of the lightest (SM-like) Higgs boson is not a free parameter, but depends crucially on the top-squark masses and the mixing parameter $X_t = A_t - \mu/\tan\beta$. Consequently, the experimental signal for

[1] This bound does not hold if $m_{\tilde{t}_1} - m_{\tilde{\chi}_1^0} \simeq m_t, m_W + m_b$. These regions in the parameter space are not yet covered by the experimental searches, due to the large $t\bar{t}$ background.

a Higgs boson with a mass around 125 GeV yields a strong constraint for the scalar-top sector that has to be taken into account in any phenomenological studies. In general, the Higgs-mass constraint requires heavy stops and/or large mixing in the stop sector. Finally, a consistent computation at NLO EW accuracy requires a PDF set which includes both the photon structure function and the QED contributions to the evolution equations. When the study in Ref. [19] was performed, the `MRST2004QED` set [72] was the only one fulfilling this requirement. This set is affected by large uncertainties that have been significantly reduced in the newly available `NNPDF2.3QED` PDF set [73]. Here, latest data from deep inelastic scattering and from the LHC are included. It is worth to investigate how the new PDF alters the EW corrections to the production of the lightest top-squark.

Our study mainly focuses on the NLO corrections to the inclusive stop–anti-stop production cross section, including corrections of electroweak origin. This analysis can be directly used in experimental analyses to estimate the theoretical uncertainty related to the missing EW corrections. Besides corrections to inclusive cross sections we also consider the impact of the electroweak corrections on several kinematic distributions, which may be significant in specific SUSY scenarios [19].

This paper is structured as follows. Section 2 reviews the calculation of the total cross section of stop–anti-stop pair production, including both NLO QCD and NLO EW contributions. Section 3 is dedicated to the presentation of the numerical results, followed by our conclusions in Section 4.

2. Computational details

The leading-order contribution to the hadronic cross section for the production of stop–anti-stop pairs is of the $\mathcal{O}\left(\alpha_s^2\right)$, described as follows,

$$\sigma^{\mathrm{LO}}_{pp\to\tilde{t}_1\tilde{t}_1^*} = \sigma^{2,0}_{gg\to\tilde{t}_1\tilde{t}_1^*} + \sum_q \sigma^{2,0}_{q\bar{q}\to\tilde{t}_1\tilde{t}_1^*}\,, \tag{2.1}$$

indicating the perturbative order $\mathcal{O}\left(\alpha_s^a\,\alpha^b\right)$ of the partonic processes X contributing to the total hadronic cross section as $\sigma_X^{a,b}$. The sum in Eq. (2.1) runs over the four lightest quark flavors, $q = u, d, c, s$. We neglect the bottom-initiated partonic processes, since they are suppressed by the bottom-quark parton distribution function and turn out to be small [28, 32].[2] The partonic cross sections for the gg and $q\bar{q}$ channel can be found in Eq. (3) and Eq. (4) of [15], respectively. They depend only on the mass of the produced top-squarks.

The NLO QCD contributions, of $\mathcal{O}\left(\alpha_s^3\right)$, are given by

$$\Delta\sigma^{\mathrm{QCD}}_{pp\to\tilde{t}_1\tilde{t}_1^*} = \sigma^{3,0}_{gg\to\tilde{t}_1\tilde{t}_1^*} + \sigma^{3,0}_{gg\to\tilde{t}_1\tilde{t}_1^* g} \tag{2.2}$$

[2] Large contributions from the $b\bar{b}$ channel quoted in Ref. [23] are a consequence of resonant Higgs-boson exchange in the s-channel, as well as Higgs–$b\bar{b}$ Yukawa couplings enhanced by the choice of a negative value for the parameter μ. In our analyses we do not consider resonant Higgs bosons or negative values of μ, which are in general disfavored by the measured value of the anomalous magnetic moment of the muon [74].

$$+ \sum_q \left(\sigma^{3,0}_{q\bar{q}\to\tilde{t}_1\tilde{t}_1^*} + \sigma^{3,0}_{q\bar{q}\to\tilde{t}_1\tilde{t}_1^* g} + \sigma^{3,0}_{qg\to\tilde{t}_1\tilde{t}_1^* q} + \sigma^{3,0}_{\bar{q}g\to\tilde{t}_1\tilde{t}_1^*\bar{q}} \right).$$

They have been computed in Ref. [15] and are implemented in the public code `Prospino` [68]. The NLO QCD corrections depend on the masses of the top squarks and of the gluino, and on the stop mixing angle.

The EW contributions arise at $\mathcal{O}\left(\alpha^2\right)$, $\mathcal{O}\left(\alpha_s\alpha\right)$ and $\mathcal{O}\left(\alpha_s^2\alpha\right)$; they can be separated into four different channels according to the partonic initial states,

$$\Delta\sigma^{\text{EW}}_{pp\to\tilde{t}_1\tilde{t}_1^*} = \Delta\sigma^{\text{EW}\ gg}_{pp\to\tilde{t}_1\tilde{t}_1^*} + \Delta\sigma^{\text{EW}\ q\bar{q}}_{pp\to\tilde{t}_1\tilde{t}_1^*} + \Delta\sigma^{\text{EW}\ qg}_{pp\to\tilde{t}_1\tilde{t}_1^*} + \Delta\sigma^{\text{EW}\ g\gamma}_{pp\to\tilde{t}_1\tilde{t}_1^*}\,, \tag{2.3}$$

with

$$\begin{aligned}
\Delta\sigma^{\text{EW}\ gg}_{pp\to\tilde{t}_1\tilde{t}_1^*} &= \sigma^{2,1}_{gg\to\tilde{t}_1\tilde{t}_1^*} + \sigma^{2,1}_{gg\to\tilde{t}_1\tilde{t}_1^*\gamma}\,,\\
\Delta\sigma^{\text{EW}\ q\bar{q}}_{pp\to\tilde{t}_1\tilde{t}_1^*} &= \sum_q \left(\sigma^{0,2}_{q\bar{q}\to\tilde{t}_1\tilde{t}_1^*} + \sigma^{2,1}_{q\bar{q}\to\tilde{t}_1\tilde{t}_1^*} + \sigma^{2,1}_{q\bar{q}\to\tilde{t}_1\tilde{t}_1^* g} + \sigma^{2,1}_{q\bar{q}\to\tilde{t}_1\tilde{t}_1^*\gamma} \right),\\
\Delta\sigma^{\text{EW}\ qg}_{pp\to\tilde{t}_1\tilde{t}_1^*} &= \sum_q \left(\sigma^{2,1}_{qg\to\tilde{t}_1\tilde{t}_1^* q} + \sigma^{2,1}_{\bar{q}g\to\tilde{t}_1\tilde{t}_1^*\bar{q}} \right),\\
\Delta\sigma^{\text{EW}\ g\gamma}_{pp\to\tilde{t}_1\tilde{t}_1^*} &= \sigma^{1,1}_{g\gamma\to\tilde{t}_1\tilde{t}_1^*}\,.
\end{aligned} \tag{2.4}$$

In principle these electroweak terms depend on the full set of MSSM parameters. We compute them by using `FeynArts` [75,76] and `FormCalc` [76,77], together with `LoopTools` [76] for the numerical evaluation of the one-loop integrals. Ultraviolet divergences are cancelled by renormalization at the electroweak one-loop level, along the lines of Ref. [28]. Infrared and collinear singularities are handled by using mass regularization and are computed by using the double cut-off phase-space-slicing method [78–80], as described in Ref. [24]. The initial-state collinear singularities of gluonic (photonic) origin are factorized and absorbed in the parton distribution functions by using the $\overline{\text{MS}}$ (DIS) scheme. Our computation has been numerically checked against the results presented in [19]. The EW contributions have been implemented in the code `SusyHell`, a (to be public) Monte Carlo integrator for the production of colored SUSY particles at the LHC.

The inclusive cross section for stop–anti-stop production, complete at NLO, is obtained by summing the LO cross section, Eq. (2.1), and the NLO contributions, Eqs. (2.2) and (2.3). For a discussion of the QCD and EW effects separately, it is convenient to define the individual and summed cross-section parts as follows,

$$\sigma^{\text{NLO QCD}}_{pp\to\tilde{t}_1\tilde{t}_1^*} = \sigma^{\text{LO}}_{pp\to\tilde{t}_1\tilde{t}_1^*} + \Delta\sigma^{\text{QCD}}_{pp\to\tilde{t}_1\tilde{t}_1^*}\,, \tag{2.5a}$$

$$\sigma^{\text{NLO EW}}_{pp\to\tilde{t}_1\tilde{t}_1^*} = \sigma^{\text{LO}}_{pp\to\tilde{t}_1\tilde{t}_1^*} + \Delta\sigma^{\text{EW}}_{pp\to\tilde{t}_1\tilde{t}_1^*}\,, \tag{2.5b}$$

$$\sigma^{\text{NLO}}_{pp\to\tilde{t}_1\tilde{t}_1^*} = \sigma^{\text{LO}}_{pp\to\tilde{t}_1\tilde{t}_1^*} + \Delta\sigma^{\text{QCD}}_{pp\to\tilde{t}_1\tilde{t}_1^*} + \Delta\sigma^{\text{EW}}_{pp\to\tilde{t}_1\tilde{t}_1^*}\,, \tag{2.5c}$$

to be used in the numerical studies of the next section.

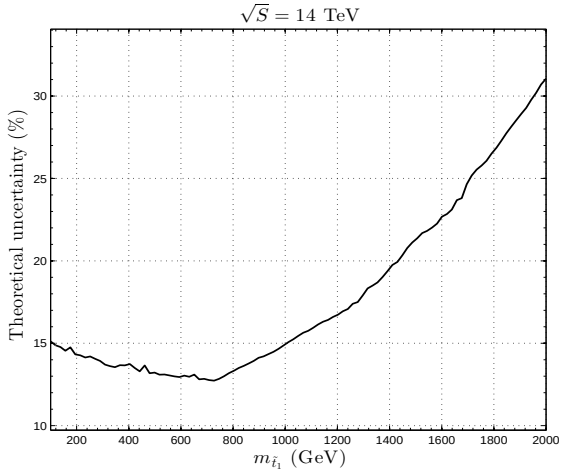

Figure 1: Theoretical uncertainty on the total cross section for $\tilde{t}_1\tilde{t}_1^*$ production at the LHC. It has been computed by using the code `NLL-fast` [33] and the procedure described in Ref. [69].

3. Numerical analysis

The numerical values of the Standard Model input parameters are chosen according to

$$\begin{aligned} m_{\rm Z} &= 91.1876 \text{ GeV}\,, & m_{\rm W} &= 80.425 \text{ GeV}\,, \\ m_t &= 173.2 \text{ GeV}\,, & m_b^{\overline{\rm MS}}(m_{\rm Z}) &= 2.94 \text{ GeV}\,, \\ \alpha^{-1} &= 137.036\,, & \alpha_s(m_{\rm Z}) &= 0.119\,. \end{aligned} \tag{3.1}$$

The results presented in this section are computed for a hadronic center-of-mass energy of $\sqrt{S} = 14$ TeV. For the numerical evaluation of the hadroinc cross sections, we use the `NNPDF2.3QED` PDF set [73]. The latter has been implemented in `Prospino` and `SusyHell` through the `LHAPDF` interface [81], which also automatically accounts for the consistent evolution of the strong coupling constant. The factorization scale $\mu_{\rm F}$ and the renormalization scale $\mu_{\rm R}$ are set to a common value, equal to the mass of the lightest top-squark, $\mu_{\rm F} = \mu_{\rm R} = m_{\tilde{t}_1}$.

In the following we consider various phenomenological MSSM scenarios characterized by ten TeV-scale free parameters,

$$m_{A_0}\,, \quad \tan\beta\,, \quad X_t\,, \quad \mu\,, \quad M_2\,, \quad m_{\tilde{g}}\,, \quad M_{\tilde{q}_{1,2}}\,, \quad M_{\tilde{\ell}_{1,2}}\,, \quad M_{\tilde{q}_3}\,, \quad M_{\tilde{\ell}_3}\,, \tag{3.2}$$

from which the individual soft-breaking parameters are obtained in the following simplified way:

$$\begin{aligned} &M_{\tilde{t},{\rm L}} = M_{\tilde{t},{\rm R}} = M_{\tilde{b},{\rm R}} = M_{\tilde{q}_3}\,, \quad M_{\tilde{f},{\rm L}} = M_{\tilde{f},{\rm R}} = M_{\tilde{q}_{1,2}}\,, \quad (f = u,d,c,s)\,, \\ &M_{\tilde{\tau},{\rm L}} = M_{\tilde{\tau},{\rm R}} = M_{\tilde{\nu}_\tau,{\rm R}} = M_{\tilde{\ell}_3}\,, \quad M_{\tilde{f},{\rm L}} = M_{\tilde{f},{\rm R}} = M_{\tilde{\ell}_{1,2}}\,, \quad (f = e,\mu,\nu_e,\nu_\mu)\,, \\ &M_1 = \frac{5}{3}\frac{s_{\rm W}^2}{c_{\rm W}^2} M_2\,, \qquad\qquad A_f = X_t - \frac{\mu}{\tan\beta}\,, \qquad (f = e,\mu,\tau,u,d,c,s,b,t)\,; \end{aligned} \tag{3.3}$$

thereby, for M_1 gaugino-mass unification at the GUT scale is assumed. From these soft parameters we calculate the physical spectrum using tree-level relations. The only exception is the physical mass of the Higgs bosons, computed by using the code `FeynHiggs 2.10` [82–86].

3.1 Total cross section

For our numerical evaluation we consider several benchmark scenarios as defined below. Within these scenarios we perform various one-dimensional scans over the parameters listed in (3.2). In these scans we focus on regions allowed by limits from the Higgs sector, i.e. we require a Higgs-state close to the observed one, with couplings compatible with the observed rates in the Higgs search channels. The compatibility between the considered models and the experimental results has been checked by using the codes `HiggsBounds` [87–90] and `HiggsSignals` [91]. They compute a χ^2 measure from the predictions of the model and the measured Higgs rates and masses. From this measure a p-value is estimated, testing the consistency between the model and the data. As a practical rejection criterion, we discard a model point if the corresponding p-value is below 0.0027, i.e. we require consistency at the three-sigma level.

The results of the scans are shown in Figs. 2-8. Each Figure collects six plots related to two different scans. In the upper plots, (a) and (b), we show the inclusive LO cross section defined in Eq. (2.1) and the NLO cross section predictions defined in Eqs. (2.5). The yield of the NLO contribution relative to the LO cross section is displayed as well. The panels (c) and (d) show the individual EW contributions of the various channels defined in Eqs. (2.4) as well as the total NLO EW contribution, Eq. (2.5b). They also show the impact of the various channels relative to the LO cross section. Panels (e) and (f) display the variation of the mass of the produced $\tilde{t}_1$.

Light-Higgs scenario This scenario is inspired by the best-fit point of Ref. [92]. In that study a fit of phenomenological MSSM scenarios compatible with electroweak precision observables and with experimental searches at the LHC and the Tevatron was performed. The values of the parameters characterizing this scenario are shown in Table 1(a). The left (right) panels of Fig. 2 show the results of the scan over X_t ($M_{\tilde{q}_3}$), and Fig. 3 displays the results of two scans over μ. Additional scans over M_2 and $m_{\tilde{g}}$ are very insensitive to the values of these parameters and we do not include them here.

The dependence of the total cross section on X_t is mild and basically related to the dependence of $m_{\tilde{t}_1}$ on X_t. On the other hand, the total cross section depends strongly on $M_{\tilde{q}_3}$ and varies over four orders of magnitude in the considered parameter range, cfr. Fig. 2(b). For $M_{\tilde{q}_3} \geq 1400$ GeV ($m_{\tilde{t}_1} \geq 1300$ GeV) the NLO cross section drops below 1 fb. Correspondingly high luminosities are required to exclude this scenario. In the high $M_{\tilde{q}_3}$ region the relative impact of the EW corrections become more important, up to $20 - 30\%$ of the LO cross section. The relative impact of the EW corrections is enhanced by the behavior of the QCD corrections whose relative yield decreases from 50 to 40% above the $\tilde{t}_1 \to \tilde{g}t$ threshold, $M_{\tilde{q}_3} \simeq 1300$ GeV. As can be inferred from Fig. 2(d), the EW corrections from the $q\bar{q}$ and qg channels are negligible, while the ones from the gg-channel

m_{A_0}	669 GeV	$\tan\beta$	16.5
X_t	2000 GeV	μ	2640 GeV
M_2	201 GeV	$m_{\tilde{g}}$	1000 GeV
$M_{\tilde{q}_{1,2}}$	1000 GeV	$M_{\tilde{\ell}_{1,2}}$	300 GeV
$M_{\tilde{q}_3}$	1000 GeV	$M_{\tilde{\ell}_3}$	285 GeV

(a) Light-Higgs scenario

m_{A_0}	700 GeV	$\tan\beta$	20
X_t	$2M_{\tilde{q}_3}$	μ	350 GeV
M_2	350 GeV	$m_{\tilde{g}}$	1500 GeV
$M_{\tilde{q}_{1,2}}$	1500 GeV	$M_{\tilde{\ell}_{1,2}}$	500 GeV
$M_{\tilde{q}_3}$	500 GeV	$M_{\tilde{\ell}_3}$	1000 GeV

(b) Light-stop scenario

m_{A_0}	700 GeV	$\tan\beta$	20
X_t	$1.6\,M_{\tilde{q}_3}$	μ	500 GeV
M_2	200 GeV	$m_{\tilde{g}}$	1500 GeV
$M_{\tilde{q}_{1,2}}$	1500 GeV	$M_{\tilde{\ell}_{1,2}}$	500 GeV
$M_{\tilde{q}_3}$	1000 GeV	$M_{\tilde{\ell}_3}$	245 GeV

(c) Light-stau scenario

m_{A_0}	800 GeV	$\tan\beta$	15
X_t	$2.45\,M_{\tilde{q}_3}$	μ	2000 GeV
M_2	200 GeV	$m_{\tilde{g}}$	1500 GeV
$M_{\tilde{q}_{1,2}}$	1500 GeV	$M_{\tilde{\ell}_{1,2}}$	500 GeV
$M_{\tilde{q}_3}$	1000 GeV	$M_{\tilde{\ell}_3}$	500 GeV

(d) Tau-phobic scenario

m_{A_0}	800 GeV	$\tan\beta$	30
X_t	$1.5\,M_{\tilde{q}_3}$	μ	200 GeV
M_2	200 GeV	$m_{\tilde{g}}$	1500 GeV
$M_{\tilde{q}_{1,2}}$	1500 GeV	$M_{\tilde{\ell}_{1,2}}$	500GeV
$M_{\tilde{q}_3}$	1000 GeV	$M_{\tilde{\ell}_3}$	1000 GeV

(e) $m_h^{\text{mod }+}$ scenario

m_{A_0}	800 GeV	$\tan\beta$	30
X_t	$-1.9\,M_{\tilde{q}_3}$	μ	200 GeV
M_2	200 GeV	$m_{\tilde{g}}$	1500 GeV
$M_{\tilde{q}_{1,2}}$	1500 GeV	$M_{\tilde{\ell}_{1,2}}$	500 GeV
$M_{\tilde{q}_3}$	1000 GeV	$M_{\tilde{\ell}_3}$	1000 GeV

(f) $m_h^{\text{mod }-}$ scenario

Table 1: Benchmark scenarios within our ten-parameter phenomenological MSSM.

are of the order of 5% of the LO cross section, irrespective to the value of $M_{\tilde{q}_3}$. In this scan the $g\gamma$-channel dominates the EW corrections for $M_{\tilde{q}_3} \geq 1000$ GeV. Its inclusion in experimental studies would significantly reduce the theoretical uncertainties, i.e. the systematic uncertainty originated from neglecting the EW corrections.

The LO and NLO QCD cross section is independent of μ, see Fig. 3(a) and Fig. 3(b). However, the NLO EW and thus also the full NLO cross section do depend on μ. The NLO EW corrections double their impact on the LO cross section when μ varies from 500 to 2500 GeV. In the left part of Fig. 3, where we take $M_{\tilde{q}_3} = 1000$ GeV, their contributions are below 15%, i.e. four times smaller than those of the QCD corrections. The right scan, where we assume $M_{\tilde{q}_3} = 1250$ GeV, exhibits larger EW corrections: they amount to more than 15% of the LO cross section for $\mu \geq 1500$ GeV. The relative impact of the various channels of the EW corrections for $M_{\tilde{q}_3} = 1000$ GeV and $M_{\tilde{q}_3} = 1260$ GeV is shown in Fig. 3(c) and Fig. 3(d) respectively. Again, the $q\bar{q}$ and gq-channel are negligible, while the contribution of the $g\gamma$-channel is constant and larger for $M_{\tilde{q}_3} = 1260$ GeV. In the $M_{\tilde{q}_3} = 1000$ (1250) GeV scan this channel contributes about 7% (11%) of the LO cross section. Instead, the contributions from the gg-channel strongly depend on μ and increase as this parameter increases. For $M_{\tilde{q}_3} = 1000$ GeV it dominates the EW corrections for $\mu \geq 2700$ GeV. It is worth to note that in both cases the inclusion of the tree-level,

model-independent $g\gamma$-channel would significantly reduce the EW theoretical uncertainty. In these scans we observe a $\tilde{t}_1 \to \tilde{\chi}_3^0 t$ threshold at $\mu \simeq 650$ (950) GeV for $M_{\tilde{q}_3} = 1000$ (1250) GeV.

Light-stop scenario This scenario has been defined in Ref. [93] in correspondence to the values of the parameters summarized in Table 1(b). The value of $M_{\tilde{q}_3}$ is significantly below the TeV-scale, while X_t is chosen to maximize the mass of the lightest CP-even Higgs boson h, leading to a phenomenologically-viable scenario with a light stop.

The dependence of the total cross section on $M_{\tilde{q}_3}$ is shown in Fig. 4(a). Both the LO and the NLO cross section depend strongly on this parameter: their values span three orders of magnitude when $M_{\tilde{q}_3}$ varies from 400 to 1000 GeV. The relative impact of the QCD corrections is large, while its dependence on $M_{\tilde{q}_3}$ is mild: over the entire $M_{\tilde{q}_3}$ interval they are $50-55\%$ of the LO cross section. Outside the $\tilde{t}_1 \to \tilde{\chi}_4^0 t$ threshold region, the EW corrections are positive and small, i.e. they are 8% of the LO cross section at most. The relative impact of the EW corrections of the different channels as a function of $M_{\tilde{q}_3}$ is shown in Fig. 4(c). Outside of the threshold region the bulk of the EW contributions originate from the $g\gamma$-channel, owing to mutual cancellations between the gg- and the $q\bar{q}$-channels.

Fig. 4(b) shows the dependence of the total cross section on μ. The LO and NLO total cross sections are independent of the value of μ in a vast portion of the scanned region. The total NLO cross section decreases in the high μ region, i.e. $\mu \geq 1200$ GeV, as a consequence of the decrease of the EW corrections. The variation is below 10% and it takes place when approaching the $\tilde{t}_1 \to \tilde{b}_1 W$ threshold located in the phenomenologically excluded region, $M_{\tilde{q}_3} \geq 1780$ GeV.

As can be inferred from Fig. 4(d), the $g\gamma$-channel dominates in the $\mu = 300-600$ GeV range. For higher values of this parameter, $\mu = 700-1200$ GeV, the gg- and the $g\gamma$-channel dominate and result in an overall negative NLO EW correction. The inclusion of the $g\gamma$-channel only would thus overestimate the impact of the EW corrections.

Light-stau scenario This scenario exhibits a sizable mixing in the $\tilde{\tau}$ sector and a rather low value of $M_{\tilde{\ell}_3}$, allowing for a light $\tilde{\tau}$ state and a possible enhancement of the $h \to \gamma\gamma$ decay rate compared to its SM prediction [93]. The value of the parameters characterizing this scenario are listed in Table 1(c).

In the left (right) plots of Fig. 5 we investigate the dependence on $M_{\tilde{q}_3}$ (μ) within this scenario. The NLO QCD corrections to the total cross section do only marginally depend on $M_{\tilde{q}_3}$ and negligibly on μ. They amount to 50% of the LO cross section, cfr. Fig. 5(a) and 5(b).

The dependence of the EW contributions on $M_{\tilde{q}_3}$ is less trivial. Below the $\tilde{t}_1 \to \tilde{\chi}_3^0 t$ threshold at $M_{\tilde{q}_3} \simeq 800$ GeV the EW corrections are flat and small, below 5% of the LO cross section. Above the threshold the corrections grow as $M_{\tilde{q}_3}$ grows reaching 10% (15%) of the LO cross section for $M_{\tilde{q}_3} \simeq 1150$ (1200) GeV, i.e. for $m_{\tilde{t}_1} \simeq 1050$ (1200) GeV. In the high $M_{\tilde{q}_3}$ region the cross section prediction is thus substantially modified by the inclusion of the EW corrections. As shown in Fig. 5(c), outside the threshold region the EW contributions are decently approximated by the $g\gamma$-channel only; indeed, the other channels contribute only up to 2% of the LO cross section.

Here, the EW corrections are only mildly affected by the variation of μ, cfr. Fig. 5(b). Far from the threshold region, $\mu \simeq 700$ GeV, they are flat and of the order of $7-10\%$ of the LO cross section. The leading contribution to the EW corrections is the $\mu-$independent contribution of the $g\gamma$-channel, which below (above) the threshold is slightly (considerably) enhanced by the other channels.

Tau-phobic scenario This scenario belongs to the two-parameter family of scenarios also introduced in [93]; here we define it by the parameters listed in Table 1(d). An intermediate value of $M_{\tilde{\ell}_3}$ together with a large value of μ lead to a somewhat suppressed $h \to \tau^+\tau^-$ decay rate, while all other Higgs observables remain SM-like.

The relative size of the QCD corrections, about 50% of the LO the cross section, is not affected by the variation of either $M_{\tilde{q}_3}$ or μ, see Figs. 6(a) and 6(b). The EW contributions, on the other hand, do depend on $M_{\tilde{q}_3}$; their relative size is tripled when $M_{\tilde{q}_3}$ varies from 1000 to 1800 GeV. Hence, the EW corrections are important and not negligible; they are more than 10% of the LO cross section over almost the entire region of $M_{\tilde{q}_3}$ considered, i.e. $M_{\tilde{q}_3} \geq 1100$ GeV or, equivalently, $m_{\tilde{t}_1} \geq 900$ GeV. Moreover they can be as large as 25% of the LO cross section in the large $M_{\tilde{q}_3}$ region, $M_{\tilde{q}_3} \geq 1700$ GeV.

The dependence of the EW corrections on μ is milder but nevertheless significant. The EW contributions relative to the LO cross section increase for increasing μ and double their value as μ varies from 100 to 3000 GeV reaching 10% at $\mu \simeq 2500$ GeV, cfr. Fig. 6(b).

In the considered parameter region mutual cancellations between the gg and $q\bar{q}$ channels render the $g\gamma$-channel the dominant one. Its inclusion would considerably lower the remaining EW theoretical uncertainty down to 5% of the LO cross section. The detailed behavior, however, strongly depends on μ, as can be inferred from Fig. 6(d). In particular approximating the EW contributions by just the $g\gamma$-channel becomes less and less accurate for increasing μ: the $g\gamma$-channel yields less than half of the EW corrections for $\mu \geq 2000$ GeV.

$\mathbf{m_h^{mod\pm}}$ scenarios These scenarios are defined in Ref. [93] as modifications of the $m_h^{\rm max}$ scenario [94]. They lead to a smaller mass of the lightest CP-even Higgs boson by reducing the ratio

$$r_t \equiv \left| \frac{X_t}{M_{\tilde{q}_3}} \right| .$$

The input parameters of the $m_h^{\rm mod\,+}$ and of the $m_h^{\rm mod\,-}$ scenario are collected in Table 1(e) and Table 1(f), respectively. They differ in the value of r_t and in the sign of X_t.

The dependence of the NLO corrections on $M_{\tilde{q}_3}$ in both scenarios is similar to the scenarios investigated before, see Fig. 7(a) and Fig. 8(a). The QCD corrections stay at 50% of the LO cross section over the entire $M_{\tilde{q}_3}$ interval. The relative impact of the EW corrections increases with $M_{\tilde{q}_3}$. They are larger than 10% of the LO cross section for $M_{\tilde{q}_3} \geq 1100$ GeV, that is for $m_{\tilde{t}_1}$ larger than 950 GeV. As shown in Fig. 7(c) and Fig. 8(c) mutual cancellations between the $q\bar{q}$ and gg-channel effects make the EW corrections effectively equal to the contribution of the $g\gamma$-channel.

Fig. 7(b) shows the μ-dependence of the NLO contributions in the $m_h^{\rm mod\,+}$ scenario. Outside the $\tilde{t}_1 \to \tilde{\chi}_4^0 t$ and the $\tilde{t}_1 \to \tilde{b}_1 W$ threshold region, located at $\mu \simeq 710$ GeV and

$\mu \simeq 2620$ GeV respectively, the EW corrections relative to the LO cross section are almost flat and vary from 8% to 12% as μ varies in the considered interval. As can be inferred from Fig. 7(d), the largest EW contribution originates from the $g\gamma$-channel. Outside the threshold regions the combined effect of the other channels are 2% of the LO cross section at most.

In the $m_h^{\rm mod\,-}$ scenario the relative yield of the EW corrections doubles its value from 7% to 15% as μ varies from 100 to 3000 GeV. In the low μ region, i.e. below the $\tilde{t}_1 \to \tilde{\chi}_4^0 t$ threshold at $\mu \simeq 700$ GeV, the $g\gamma$-channel is a good approximation of the EW corrections. Above the threshold its importance is reduced by the increase of the corrections of the gg-channel, which become dominant in the region $\mu \geq 2500$ GeV.

3.2 Differential distributions

In the previous subsection we studied the numerical impact of the next-to-leading order contributions to the total cross section for stop–anti-stop production at the LHC combining contributions of EW and QCD origin. Although the current experimental studies account for the higher order corrections by re-weighting the events generated at LO with the NLO(+NLL) predictions for the total rate, it is well known that higher-order contributions can significantly alter the shape of kinematic distributions.

In this subsection we study the impact of the EW corrections on differential distributions with respect to the invariant mass, the transverse momentum and the pseudo-rapidity, defined as

$$M_{\rm inv} \equiv \sqrt{\left(p_{\tilde{t}_1} + p_{\tilde{t}_1^*}\right)^2}, \qquad p_T \equiv \max\left(p_{T\,\tilde{t}_1}\,,\, p_{T\,\tilde{t}_1^*}\right), \quad \eta \equiv \begin{cases} \eta_{\tilde{t}_1} & \text{if} \quad |\eta_{\tilde{t}_1}| \geq |\eta_{\tilde{t}_1^*}| \\ \eta_{\tilde{t}_1^*} & \text{if} \quad |\eta_{\tilde{t}_1}| < |\eta_{\tilde{t}_1^*}| \end{cases},$$

respectively. The quantities p_j, $p_{T\,j}$ and η_j are the four-momentum, the transverse momentum and the pseudo-rapidity of the particle j, respectively. We have considered the six SUSY scenarios described in Table 1, but here we present results for the light-stop and for the tau-phobic scenario only, since the other scenarios exhibit similar features of the latter one. The results are collected in Fig. 9 and in Fig. 10. In the upper plots, (a) and (b), we show the LO and NLO invariant mass distribution [panel (a)], and the yield of the $\mathcal{O}(\alpha^2)$, $\mathcal{O}(\alpha_s\alpha)$ and $\mathcal{O}(\alpha_s^2\alpha)$ corrections [panel (b)]. Panels (c), (d) and panels (e), (f) show the same information for the transverse momentum and the pseudo-rapidity distributions, respectively.

Invariant mass distribution In scenarios with a heavy stop exemplified by the tau-phobic scenario in Fig. 10, the relative impact of the EW corrections to the invariant mass distributions decreases as $M_{\rm inv}$ increases. As can be inferred from Fig. 10(a) the EW corrections are positive and sizable in the small $M_{\rm inv}$ region while in the large $M_{\rm inv}$ region the EW corrections become negative. In this regime the relative impact of the corrections is almost flat and their size is small. The behavior of the EW corrections can be explained looking at the contributions of the different EW corrections collected in Fig. 10(b). The $\mathcal{O}(\alpha_s\alpha)$ and the $\mathcal{O}(\alpha_s^2\alpha)$ corrections are the numerically dominant ones. In the small $M_{\rm inv}$ region they are both positive and sum up enhancing the EW corrections. In the large $M_{\rm inv}$

region, instead, the positive $\mathcal{O}(\alpha_s\alpha)$ corrections partially compensate the large negative contributions of the $\mathcal{O}(\alpha_s^2\alpha)$ corrections.

Also in the light stop-scenario the relative yield of the EW corrections decreases as $M_{\rm inv}$ increases but, immediately above the production threshold, they become negative, see Fig. 9(a). As one can see in Fig. 9(b), this behavior is again related to mutual cancellation between the $\mathcal{O}(\alpha_s\alpha)$ and the $\mathcal{O}(\alpha_s^2\alpha)$ corrections. In the entire $M_{\rm inv}$ region the $\mathcal{O}(\alpha^2)$ corrections are irrelevant for all considered scenarios.

Transverse momentum distribution The EW corrections to the transverse momentum distribution exhibit features similar to those for the invariant mass distribution.

In the low $p_{\rm T}$ region the EW corrections are positive and sizable in all scenarios but the light-stop one, i.e. their relative yield is above 10%. For high values of $p_{\rm T}$, instead, the absolute value of the EW corrections decreases and they become negative, see Fig. 10(c). As shown in Fig. 10(d), this behavior is originated by the same interplay between the $\mathcal{O}(\alpha_s\alpha)$ and $\mathcal{O}(\alpha_s^2\alpha)$ corrections present in the $M_{\rm inv}$ distribution.

As shown in Fig. 9(c), in the light-stop scenario the relative impact of the EW corrections is below 10%. This feature can be understood by looking at the behavior of the various EW contributions, Fig. 9(d). In the low $p_{\rm T}$ region the $\mathcal{O}(\alpha_s\alpha)$ and $\mathcal{O}(\alpha_s^2\alpha)$ contributions are both positive but small, i.e. below 5%, while in the high $p_{\rm T}$ region the two contributions cancel against each other.

Pseudo-rapidity distribution As illustrated in Fig. 10(e), in all heavy-stop scenarios the EW corrections are important for large pseudo-rapidities, i.e. they are above 10% for $|\eta| \geq 2$. In the low pseudo-rapidity region the EW corrections are positive but small, and almost negligible in the central region. The behavior of the EW corrections can be understood by looking at Fig. 10(f). The large and positive $\mathcal{O}(\alpha_s\alpha)$ corrections originate from the $g\gamma$ partonic process. This process proceeds via a t- and u-channel tree-level diagram, thus it produces preferably final particles in the forward region. In this region its large contribution is further enhanced by the positive $\mathcal{O}(\alpha_s^2\alpha)$ corrections, cfr. Fig. 10(f). In the low pseudo-rapidity region, instead, the positive contributions of $\mathcal{O}(\alpha_s\alpha)$ are canceled by negative corrections of $\mathcal{O}(\alpha_s^2\alpha)$.

As shown in Fig. 9(e), in the light-stop scenario the EW corrections are generally small, i.e. below 10% for $|\eta| \leq 4$.

The importance of the EW corrections considerably depends on the kinematics of the produced $\tilde{t}_1\tilde{t}_1^*$. Thus, the yield on experimental event rates can be substantially affected by the application of kinematical cuts. Furthermore, NLO QCD corrections to the decay of the produced top-squarks may further alter significantly the shape of the kinematical distributions [57, 58]. Therefore, such NLO corrections to the decay should also be investigated systematically for the EW corrections, including EW corrections also in the decay.

4. Conclusions

In this paper we have presented the first phenomenological study for $\tilde{t}_1\tilde{t}_1^*$ production at the

LHC including both the complete NLO QCD and NLO EW contributions. We have used the most recent PDF sets including QED effects, presenting a thorough study of parameter regions compatible with a SM-like Higgs boson observed at the LHC. The allowed MSSM regions are characterized by a rather heavy $\tilde{t}_1$ and/or by a large mixing in the stop sector, i.e. large X_t.

Our analysis has shown that NLO EW contributions to $\tilde{t}_1\tilde{t}_1^*$ production are not always negligible even on an inclusive level; they can be sizable, as large as $15-20\%$ of the LO cross section, particularly in the parameter regions with heavy stops. This is mainly due to the contribution of the $g\gamma$-channel which increases with the mass of the produced top-squarks. This contribution can be easily included in the MSSM predictions for experimental investigations. Moreover, it could reduce the residual theoretical uncertainty related to the EW corrections below 5% of the LO cross section, at least in the parameter configurations where μ is not too large. The dependence on the remaining parameters of the model is found to be rather weak.

The presented study was performed using the Monte Carlo integrator `SusyHell`. This code includes the NLO EW corrections to all squark and gluino production channels and it will be made public in the future. It will allow for detailed phenomenological studies of the EW corrections to colored SUSY particle production, on an inclusive and also a fully differential level. Using this tool also the electroweak contributions should eventually be combined with higher order corrections to the decay processes.

Acknowledgments

We thank Oscar Stål for useful discussions on the code `HiggsSignals`. JML was supported by the European Commission through the "LHCPhenoNet" Initial Training Network PITN-GA-2010-264564.

References

[1] **ATLAS** Collaboration, G. Aad *et. al.*, *Observation of a new particle in the search for the Standard Model Higgs boson with the ATLAS detector at the LHC*, *Phys.Lett.* **B716** (2012) 1–29, [arXiv:1207.7214].

[2] **CMS** Collaboration, S. Chatrchyan *et. al.*, *Observation of a new boson at a mass of 125 GeV with the CMS experiment at the LHC*, *Phys.Lett.* **B716** (2012) 30–61, [arXiv:1207.7235].

[3] **LHC Higgs Cross Section Working Group** Collaboration, A. David *et. al.*, *LHC HXSWG interim recommendations to explore the coupling structure of a Higgs-like particle*, arXiv:1209.0040.

[4] **LHC Higgs Cross Section Working Group** Collaboration, S. Heinemeyer *et. al.*, *Handbook of LHC Higgs cross sections: 3. Higgs properties*, arXiv:1307.1347.

[5] **ATLAS** Collaboration. ATLAS Supersymmetry (SUSY) searches page: https://twiki.cern.ch/twiki/bin/view/AtlasPublic/SupersymmetryPublicResults.

[6] **CMS** Collaboration. CMS Supersymmetry Physics Results page: https://twiki.cern.ch/twiki/bin/view/CMSPublic/PhysicsResultsSUS.

[7] G. L. Kane and J. P. Leveille, *Experimental constraints on gluino masses and supersymmetric theories*, *Phys. Lett.* **B112** (1982) 227.

[8] P. R. Harrison and C. H. Llewellyn Smith, *Hadroproduction of supersymmetric particles*, *Nucl. Phys.* **B213** (1983) 223.

[9] E. Reya and D. P. Roy, *Supersymmetric particle production at p $\bar{p}$ collider energies*, *Phys. Rev.* **D32** (1985) 645.

[10] S. Dawson, E. Eichten, and C. Quigg, *Search for supersymmetric particles in hadron–hadron collisions*, *Phys. Rev.* **D31** (1985) 1581.

[11] H. Baer and X. Tata, *Component formulae for hadroproduction of left-handed and right-handed squarks*, *Phys. Lett.* **B160** (1985) 159.

[12] W. Beenakker, R. Hopker, M. Spira, and P. M. Zerwas, *Squark production at the Tevatron*, *Phys. Rev. Lett.* **74** (1995) 2905–2908, [hep-ph/9412272].

[13] W. Beenakker, R. Hopker, M. Spira, and P. M. Zerwas, *Gluino pair production at the Tevatron*, *Z. Phys.* **C69** (1995) 163–166, [hep-ph/9505416].

[14] W. Beenakker, R. Hopker, M. Spira, and P. M. Zerwas, *Squark and gluino production at hadron colliders*, *Nucl. Phys.* **B492** (1997) 51–103, [hep-ph/9610490].

[15] W. Beenakker, M. Krämer, T. Plehn, M. Spira, and P. M. Zerwas, *Stop production at hadron colliders*, *Nucl. Phys.* **B515** (1998) 3–14, [hep-ph/9710451].

[16] D. Goncalves-Netto, D. Lopez-Val, K. Mawatari, T. Plehn, and I. Wigmore, *Automated squark and gluino production to next-to-leading order*, *Phys.Rev.* **D87** (2013) 014002, [arXiv:1211.0286].

[17] G. Bozzi, B. Fuks, and M. Klasen, *Non-diagonal and mixed squark production at hadron colliders*, *Phys. Rev.* **D72** (2005) 035016, [hep-ph/0507073].

[18] A. T. Alan, K. Cankocak, and D. A. Demir, *Squark pair production in the MSSM with explicit CP violation*, *Phys. Rev.* **D75** (2007) 095002, [hep-ph/0702289].

[19] W. Hollik, M. Kollar, and M. K. Trenkel, *Hadronic production of top-squark pairs with electroweak NLO contributions*, *JHEP* **02** (2008) 018, [arXiv:0712.0287].

[20] S. Bornhauser, M. Drees, H. K. Dreiner, and J. S. Kim, *Electroweak contributions to squark pair production at the LHC*, *Phys. Rev.* **D76** (2007) 095020, [arXiv:0709.2544].

[21] W. Hollik, E. Mirabella, and M. K. Trenkel, *Electroweak contributions to squark–gluino production at the LHC*, *JHEP* **02** (2009) 002, [arXiv:0810.1044].

[22] S. Bornhauser, M. Drees, H. K. Dreiner, and J. S. Kim, *Rapidity gap events in squark pair production at the LHC*, *Phys. Rev.* **D80** (2009) 095007, [arXiv:0909.2595].

[23] A. Arhrib, R. Benbrik, K. Cheung, and T.-C. Yuan, *Higgs boson enhancement effects on squark-pair production at the LHC*, *JHEP* **02** (2010) 048, [arXiv:0911.1820].

[24] J. Germer, W. Hollik, E. Mirabella, and M. K. Trenkel, *Hadronic production of squark-squark pairs: the electroweak contributions*, *JHEP* **08** (2010) 023, [arXiv:1004.2621].

[25] M. Beccaria, G. Macorini, L. Panizzi, F. M. Renard, and C. Verzegnassi, *Stop-antistop and sbottom-antisbottom production at LHC: a one-loop search for model parameters dependence*, *Int. J. Mod. Phys.* **A23** (2008) 4779–4810, [arXiv:0804.1252].

[26] W. Hollik and E. Mirabella, *Squark anti-squark pair production at the LHC: the electroweak contribution*, *JHEP* **12** (2008) 087, [arXiv:0806.1433].

[27] E. Mirabella, *NLO electroweak contributions to gluino pair production at hadron colliders*, *JHEP* **12** (2009) 012, [arXiv:0908.3318].

[28] J. Germer, W. Hollik, and E. Mirabella, *Hadronic production of bottom-squark pairs with electroweak contributions*, *JHEP* **1105** (2011) 068, [arXiv:1103.1258].

[29] A. Kulesza and L. Motyka, *Threshold resummation for squark-antisquark and gluino- pair production at the LHC*, *Phys. Rev. Lett.* **102** (2009) 111802, [arXiv:0807.2405].

[30] A. Kulesza and L. Motyka, *Soft gluon resummation for the production of gluino-gluino and squark-antisquark pairs at the LHC*, *Phys. Rev.* **D80** (2009) 095004, [arXiv:0905.4749].

[31] W. Beenakker *et. al.*, *Soft-gluon resummation for squark and gluino hadroproduction*, *JHEP* **12** (2009) 041, [arXiv:0909.4418].

[32] W. Beenakker *et. al.*, *Supersymmetric top and bottom squark production at hadron colliders*, *JHEP* **08** (2010) 098, [arXiv:1006.4771].

[33] W. Beenakker, S. Brensing, M. Krämer, A. Kulesza, E. Laenen, *et. al.*, *Squark and gluino hadroproduction*, *Int.J.Mod.Phys.* **A26** (2011) 2637–2664, [arXiv:1105.1110].

[34] M. Beneke, P. Falgari, and C. Schwinn, *Colour structure in threshold resummation and squark-antisquark production at NLL*, *PoS* **EPS-HEP2009** (2009) 319, [arXiv:0909.3488].

[35] M. Beneke, P. Falgari, and C. Schwinn, *Threshold resummation for pair production of coloured heavy (s)particles at hadron colliders*, *Nucl. Phys.* **B842** (2010) [arXiv:1007.5414].

[36] P. Falgari, C. Schwinn, and C. Wever, *NLL soft and Coulomb resummation for squark and gluino production at the LHC*, *JHEP* **1206** (2012) 052, [arXiv:1202.2260].

[37] P. Falgari, C. Schwinn, and C. Wever, *Finite-width effects on threshold corrections to squark and gluino production*, *JHEP* **1301** (2013) 085, [arXiv:1211.3408].

[38] W. Beenakker, S. Brensing, M. Krämer, A. Kulesza, E. Laenen, *et. al.*, *NNLL resummation for squark-antisquark pair production at the LHC*, *JHEP* **1201** (2012) 076, [arXiv:1110.2446].

[39] A. Broggio, A. Ferroglia, M. Neubert, L. Vernazza, and L. L. Yang, *NNLL Momentum-Space Resummation for Stop-Pair Production at the LHC*, *JHEP* **1403** (2014) 066, [arXiv:1312.4540].

[40] T. Pfoh, *Phenomenology of QCD threshold resummation for gluino pair production at NNLL*, *JHEP* **1305** (2013) 044, [arXiv:1302.7202].

[41] W. Beenakker, T. Janssen, S. Lepoeter, M. Krämer, A. Kulesza, *et. al.*, *Towards NNLL resummation: hard matching coefficients for squark and gluino hadroproduction*, *JHEP* **1310** (2013) 120, [arXiv:1304.6354].

[42] W. Beenakker, C. Borschensky, M. Krämer, A. Kulesza, E. Laenen, *et. al.*, *NNLL resummation for squark and gluino production at the LHC*, arXiv:1404.3134.

[43] M. R. Kauth, J. H. Kuhn, P. Marquard, and M. Steinhauser, *Gluinonia: energy levels, production and decay*, *Nucl.Phys.* **B831** (2010) 285–305, [arXiv:0910.2612].

[44] C. Kim, A. Idilbi, T. Mehen, and Y. W. Yoon, *Production of stoponium at the LHC*, arXiv:1401.1284.

[45] K. Hagiwara and H. Yokoya, *Bound-state effects on gluino-pair production at hadron colliders*, *JHEP* **0910** (2009) 049, [arXiv:0909.3204].

[46] M. R. Kauth, J. H. Kuhn, P. Marquard, and M. Steinhauser, *Gluino pair production at the LHC: the threshold*, *Nucl.Phys.* **B857** (2012) 28–64, [arXiv:1108.0361].

[47] M. R. Kauth, A. Kress, and J. H. Kuhn, *Gluino-squark production at the LHC: the threshold*, *JHEP* **1112** (2011) 104, [arXiv:1108.0542].

[48] U. Langenfeld and S.-O. Moch, *Higher-order soft corrections to squark hadro- production*, *Phys. Lett.* **B675** (2009) 210–221, [arXiv:0901.0802].

[49] U. Langenfeld, *Threshold improved QCD corrections for stop–anti-stop production at hadron colliders*, *JHEP* **1107** (2011) 052, [arXiv:1011.3341].

[50] U. Langenfeld, S.-O. Moch, and T. Pfoh, *QCD threshold corrections for gluino pair production at hadron colliders*, *JHEP* **1211** (2012) 070, [arXiv:1208.4281].

[51] A. Broggio, A. Ferroglia, M. Neubert, L. Vernazza, and L. L. Yang, *Approximate NNLO predictions for the stop-pair production cross section at the LHC*, *JHEP* **1307** (2013) 042, [arXiv:1304.2411].

[52] W. Beenakker, R. Hopker, and P. Zerwas, *SUSY QCD decays of squarks and gluinos*, *Phys.Lett.* **B378** (1996) 159–166, [hep-ph/9602378].

[53] A. Djouadi, W. Hollik, and C. Junger, *QCD corrections to scalar quark decays*, *Phys.Rev.* **D55** (1997) 6975–6985, [hep-ph/9609419].

[54] W. Beenakker, R. Hopker, T. Plehn, and P. M. Zerwas, *Stop decays in SUSY-QCD*, *Z. Phys.* **C75** (1997) 349–356, [hep-ph/9610313].

[55] J. Guasch, W. Hollik, and J. Sola, *Full electroweak one loop radiative corrections to squark decays in the MSSM*, *Phys.Lett.* **B510** (2001) 211–220, [hep-ph/0101086].

[56] J. Guasch, W. Hollik, and J. Sola, *Fermionic decays of sfermions: a complete discussion at one loop order*, *JHEP* **0210** (2002) 040, [hep-ph/0207364].

[57] R. Boughezal and M. Schulze, *Precise predictions for top-quark plus missing energy signatures at the LHC*, *Phys.Rev.Lett.* **110** (2013), no. 19 192002, [arXiv:1212.0898].

[58] R. Boughezal and M. Schulze, *$t\bar{t}$+large missing energy from top-quark partners: a comprehensive study at next-to-leading order QCD*, *Phys.Rev.* **D88** (2013), no. 11 114002, [arXiv:1309.2316].

[59] W. Hollik, J. M. Lindert, and D. Pagani, *NLO corrections to squark-squark production and decay at the LHC*, *JHEP* **1303** (2013) 139, [arXiv:1207.1071].

[60] W. Hollik, J. M. Lindert, and D. Pagani, *On cascade decays of squarks at the LHC in NLO QCD*, *Eur.Phys.J.* **C73** (2013) 2410, [arXiv:1303.0186].

[61] R. Gavin, C. Hangst, M. Krämer, M. Muhlleitner, M. Pellen, *et. al.*, *Matching squark pair production at NLO with parton showers*, *JHEP* **10** (2013) 187, [arXiv:1305.4061].

[62] **ATLAS** Collaboration, G. Aad *et. al.*, *Search for direct top squark pair production in events with a Z boson, b-jets and missing transverse momentum in $\sqrt{s}$=8 TeV pp collisions with the ATLAS detector*, arXiv:1403.5222.

[63] **ATLAS** Collaboration, G. Aad *et. al.*, *Search for direct top-squark pair production in final states with two leptons in pp collisions at $\sqrt{s}$=8 TeV with the ATLAS detector*, arXiv:1403.4853.

[64] **ATLAS** Collaboration, G. Aad *et. al.*, *Search for direct third-generation squark pair production in final states with missing transverse momentum and two b-jets in $\sqrt{s}$ = 8 TeV pp collisions with the ATLAS detector*, *JHEP* **1310** (2013) 189, [arXiv:1308.2631].

[65] **CMS** Collaboration, S. Chatrchyan *et. al.*, *Search for stop and higgsino production using diphoton Higgs boson decays*, arXiv:1312.3310.

[66] **CMS** Collaboration, S. Chatrchyan *et. al.*, *Search for top-squark pair production in the single-lepton final state in pp collisions at $\sqrt{s}$ = 8 TeV*, *Eur.Phys.J.* **C73** (2013) 2677, [arXiv:1308.1586].

[67] **CMS** Collaboration, *Search for supersymmetry using razor variables in events with b-jets in pp collisions at 8 TeV*, Tech. Rep. CMS-PAS-SUS-13-004, CERN, Geneva, 2013.

[68] W. Beenakker, R. Hopker, and M. Spira, *PROSPINO: A program for the PROduction of Supersymmetric Particles In Next-to-leading Order QCD*, hep-ph/9611232.

[69] M. Krämer, A. Kulesza, R. van der Leeuw, M. Mangano, S. Padhi, *et. al.*, *Supersymmetry production cross sections in pp collisions at $\sqrt{s} = 7$ TeV*, arXiv:1206.2892.

[70] B. C. Allanach *et. al.*, *The Snowmass points and slopes: benchmarks for SUSY searches*, *Eur. Phys. J.* **C25** (2002) 113–123, [hep-ph/0202233].

[71] J. A. Aguilar-Saavedra *et. al.*, *Supersymmetry parameter analysis: SPA convention and project*, *Eur. Phys. J.* **C46** (2006) 43–60, [hep-ph/0511344].

[72] A. D. Martin, R. G. Roberts, W. J. Stirling, and R. S. Thorne, *Parton distributions incorporating QED contributions*, *Eur. Phys. J.* **C39** (2005) 155–161, [hep-ph/0411040].

[73] **NNPDF** Collaboration, R. D. Ball *et. al.*, *Parton distributions with QED corrections*, *Nucl.Phys.* **B877** (2013), no. 2 290–320, [arXiv:1308.0598].

[74] D. Stockinger, *The muon magnetic moment and supersymmetry*, *J. Phys.* **G34** (2007) R45–R92, [hep-ph/0609168].

[75] T. Hahn, *Generating Feynman diagrams and amplitudes with FeynArts 3*, *Comput. Phys. Commun.* **140** (2001) 418–431, [hep-ph/0012260].

[76] T. Hahn and M. Rauch, *News from FormCalc and LoopTools*, *Nucl. Phys. Proc. Suppl.* **157** (2006) 236–240, [hep-ph/0601248].

[77] T. Hahn and C. Schappacher, *The implementation of the minimal supersymmetric standard model in FeynArts and FormCalc*, *Comput. Phys. Commun.* **143** (2002) 54–68, [hep-ph/0105349].

[78] D. R. Yennie, S. C. Frautschi, and H. Suura, *The infrared divergence phenomena and high-energy processes*, *Ann. Phys.* **13** (1961) 379–452.

[79] S. Weinberg, *Infrared photons and gravitons*, *Phys. Rev.* **140** (1965) B516–B524.

[80] V. N. Baier, V. S. Fadin, and V. A. Khoze, *Quasireal electron method in high-energy quantum electrodynamics*, *Nucl. Phys.* **B65** (1973) 381–396.

[81] D. Bourilkov, R. C. Group, and M. R. Whalley, *LHAPDF: PDF use from the Tevatron to the LHC*, hep-ph/0605240.

[82] S. Heinemeyer, W. Hollik, and G. Weiglein, *The masses of the neutral CP - even Higgs bosons in the MSSM: accurate analysis at the two loop level*, *Eur.Phys.J.* **C9** (1999) 343–366, [hep-ph/9812472].

[83] S. Heinemeyer, W. Hollik, and G. Weiglein, *FeynHiggs: a program for the calculation of the masses of the neutral CP-even Higgs bosons in the MSSM*, *Comput. Phys. Commun.* **124** (2000) 76–89, [hep-ph/9812320].

[84] M. Frank *et. al.*, *The Higgs boson masses and mixings of the complex MSSM in the Feynman-diagrammatic approach*, *JHEP* **02** (2007) 047, [hep-ph/0611326].

[85] T. Hahn, S. Heinemeyer, W. Hollik, H. Rzehak, and G. Weiglein, *FeynHiggs: A program for the calculation of MSSM Higgs-boson observables - version 2.6.5*, *Comput.Phys.Commun.* **180** (2009) 1426–1427.

[86] T. Hahn, S. Heinemeyer, W. Hollik, H. Rzehak, and G. Weiglein, *High-precision predictions for the light CP-even Higgs Boson Mass of the MSSM*, arXiv:1312.4937.

[87] P. Bechtle, O. Brein, S. Heinemeyer, G. Weiglein, and K. E. Williams, *HiggsBounds: confronting arbitrary Higgs sectors with exclusion bounds from LEP and the Tevatron*, *Comput.Phys.Commun.* **181** (2010) 138–167, [arXiv:0811.4169].

[88] P. Bechtle, O. Brein, S. Heinemeyer, G. Weiglein, and K. E. Williams, *HiggsBounds 2.0.0: confronting neutral and charged Higgs sector predictions with exclusion bounds from LEP and the Tevatron*, *Comput.Phys.Commun.* **182** (2011) 2605–2631, [arXiv:1102.1898].

[89] P. Bechtle, O. Brein, S. Heinemeyer, O. Stål, T. Stefaniak, *et. al.*, *Recent developments in HiggsBounds and a preview of HiggsSignals*, *PoS* **CHARGED2012** (2012) 024, [arXiv:1301.2345].

[90] P. Bechtle, O. Brein, S. Heinemeyer, O. Stål, T. Stefaniak, *et. al.*, *HiggsBounds-4: improved tests of extended Higgs sectors against exclusion bounds from LEP, the Tevatron and the LHC*, *Eur.Phys.J.* **C74** (2014) 2693, [arXiv:1311.0055].

[91] P. Bechtle, S. Heinemeyer, O. Stål, T. Stefaniak, and G. Weiglein, *HiggsSignals: confronting arbitrary Higgs sectors with measurements at the Tevatron and the LHC*, *Eur.Phys.J.* **C74** (2014) 2711, [arXiv:1305.1933].

[92] P. Bechtle, S. Heinemeyer, O. Stål, T. Stefaniak, G. Weiglein, *et. al.*, *MSSM interpretations of the LHC discovery: light or heavy Higgs?*, *Eur.Phys.J.* **C73** (2013) 2354, [arXiv:1211.1955].

[93] M. Carena, S. Heinemeyer, O. Stål, C. Wagner, and G. Weiglein, *MSSM Higgs boson searches at the LHC: benchmark scenarios after the discovery of a Higgs-like particle*, *Eur. Phys. J.* **C73** (2013) 2552, [arXiv:1302.7033].

[94] S. Heinemeyer, W. Hollik, and G. Weiglein, *Constraints on* $\tan\beta$ *in the MSSM from the upper bound on the mass of the lightest Higgs boson*, *JHEP* **0006** (2000) 009, [hep-ph/9909540].

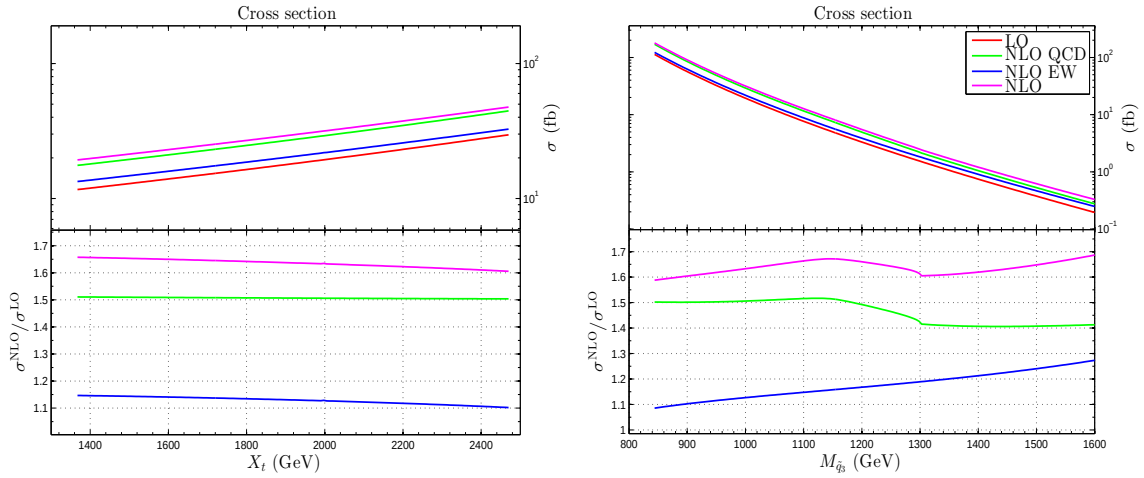

(a)

(b)

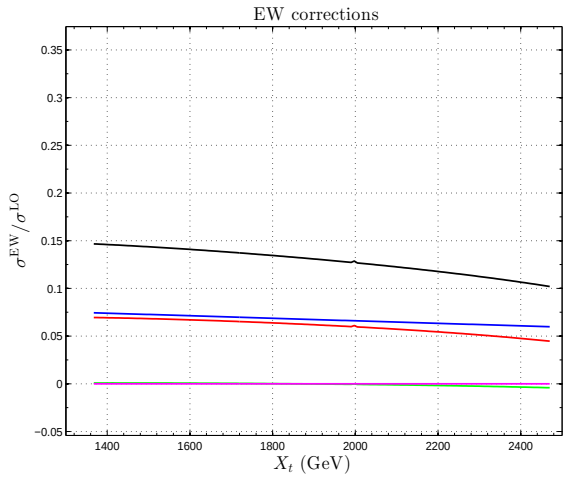

(c)

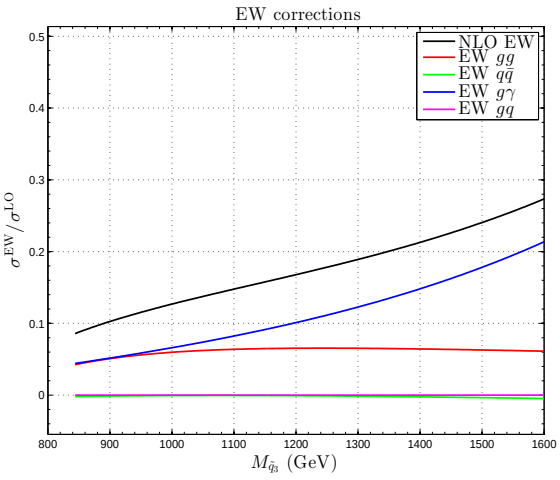

(d)

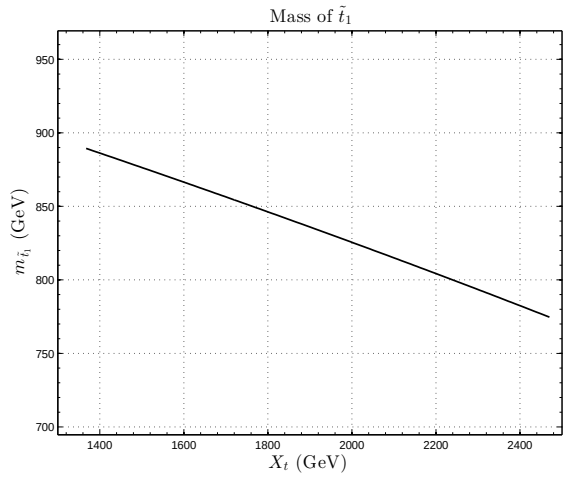

(e)

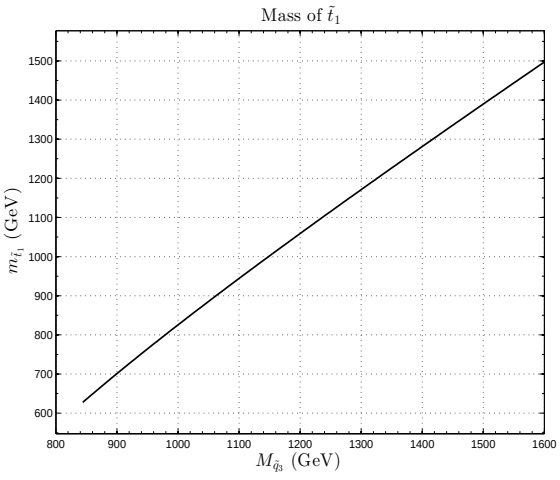

(f)

Figure 2: Left (Right) panels: scans over X_t ($M_{\tilde{q}_3}$) in the light-Higgs scenario. The value of the parameters fixed in the scans are collected in Table 1(a).

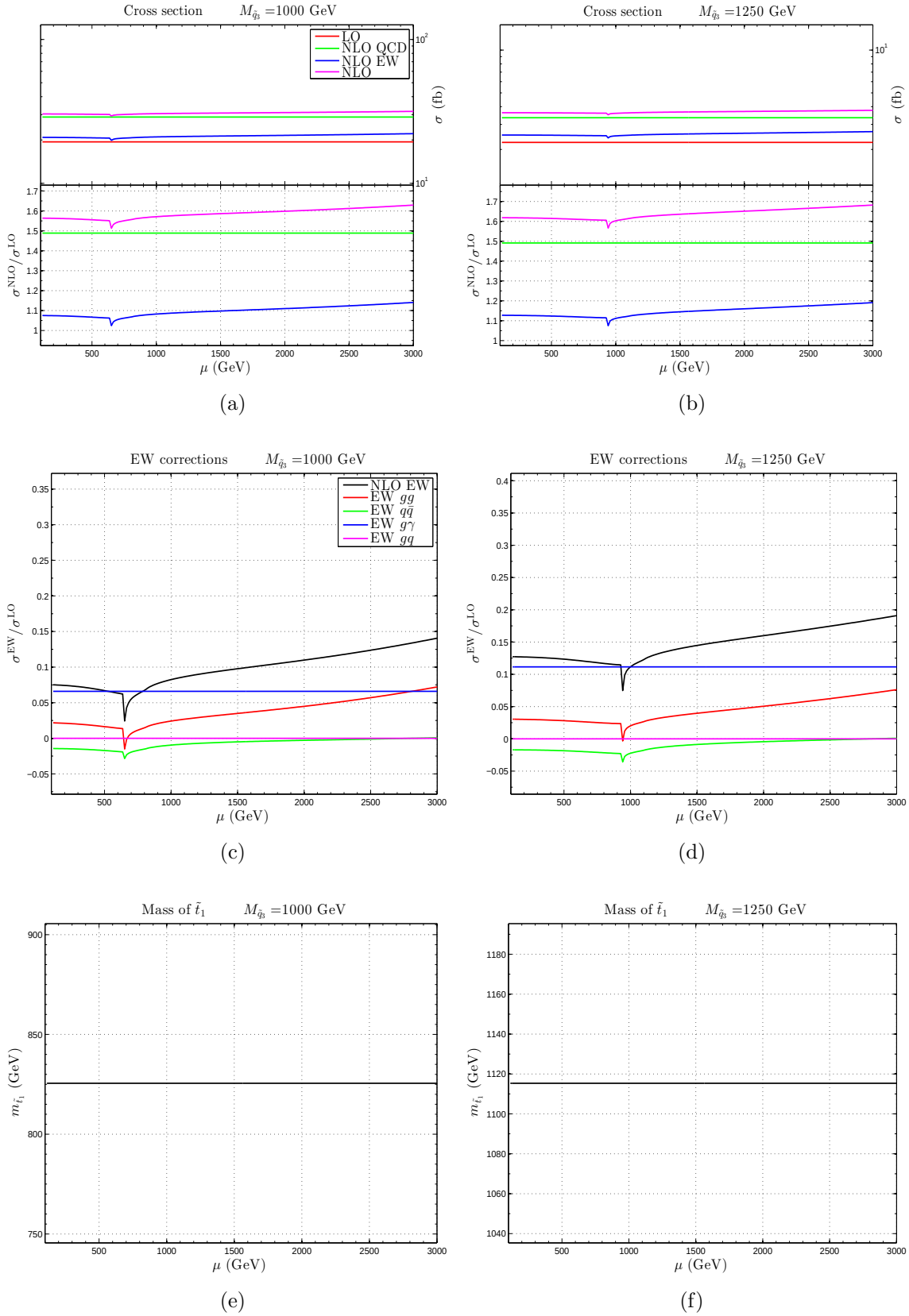

Figure 3: Scans over μ in the light-Higgs scenario. In the left (right) panel $M_{\tilde{q}_3}$ is set equal to 1000 (1260) GeV. Table 1(a) collect the value of the other parameters.

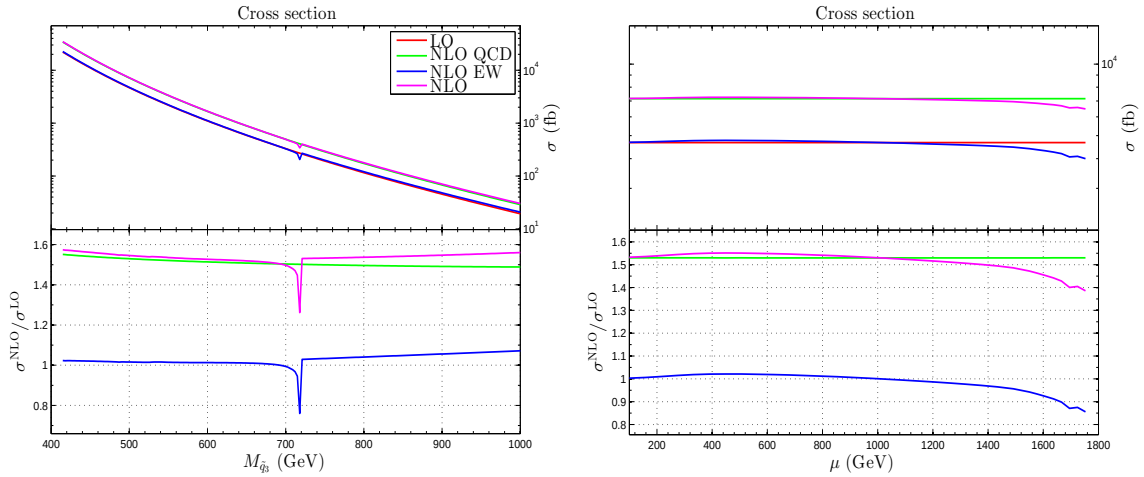

(a)

(b)

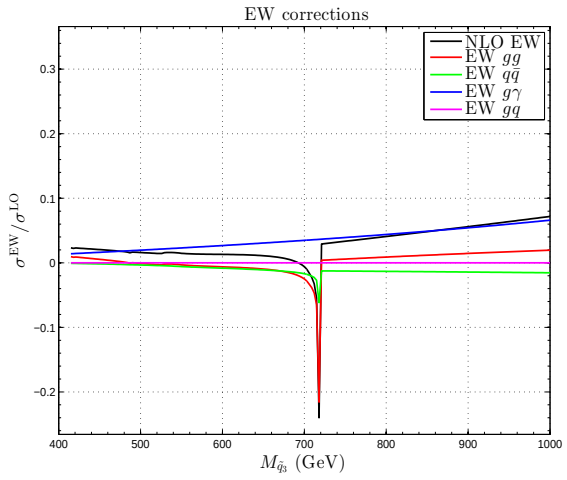

(c)

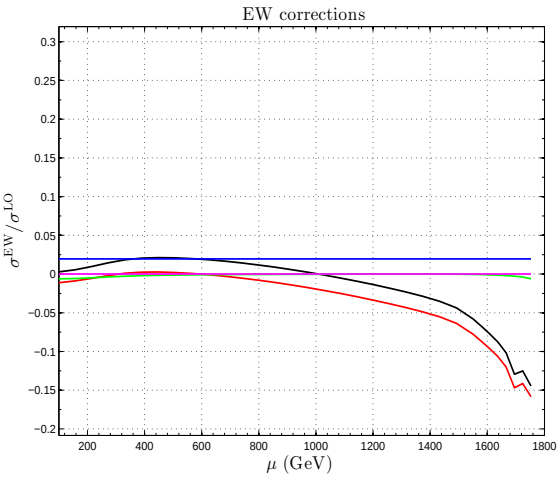

(d)

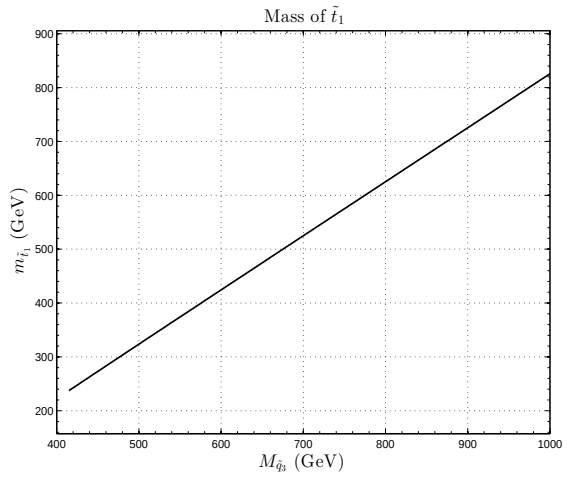

(e)

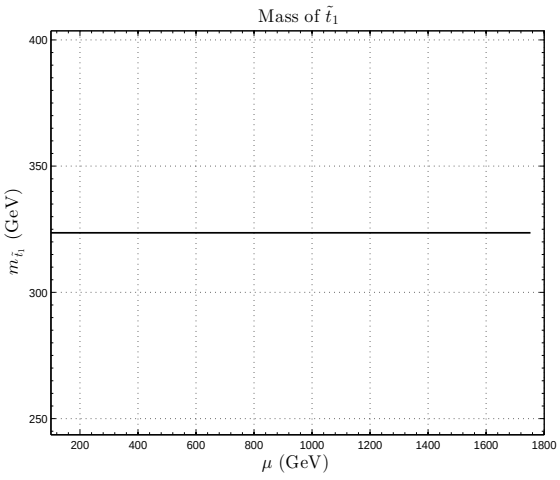

(f)

Figure 4: Left (Right) panels: scans over $M_{\tilde{q}_3}$ (μ) in the light-stop scenario. The value of the parameters not involved in the scans are collected in Table 1(b).

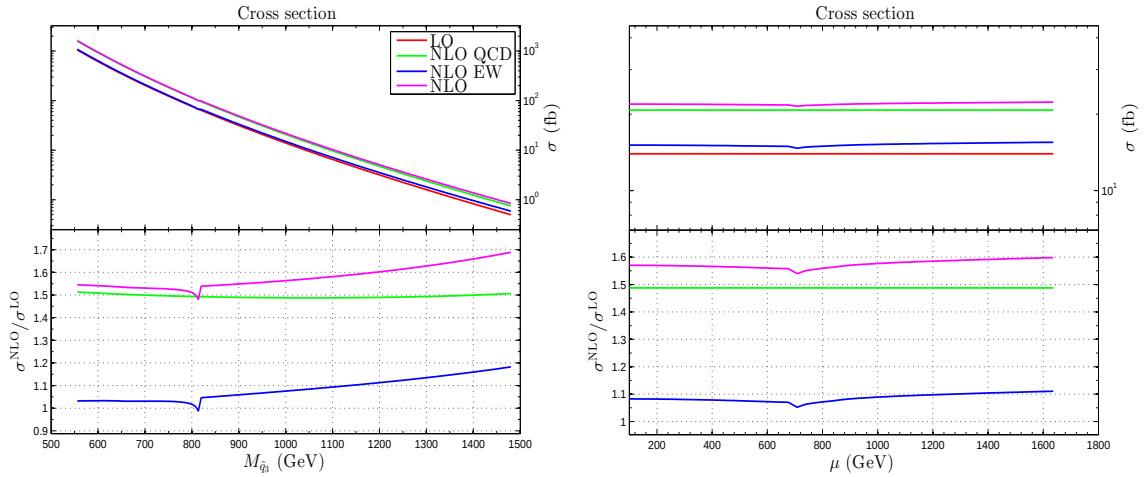

(a)

(b)

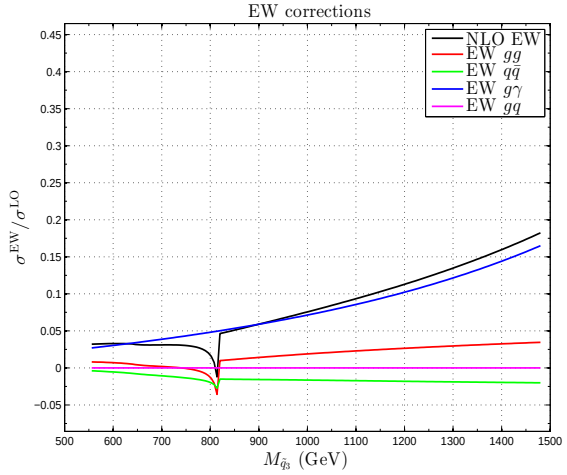

(c)

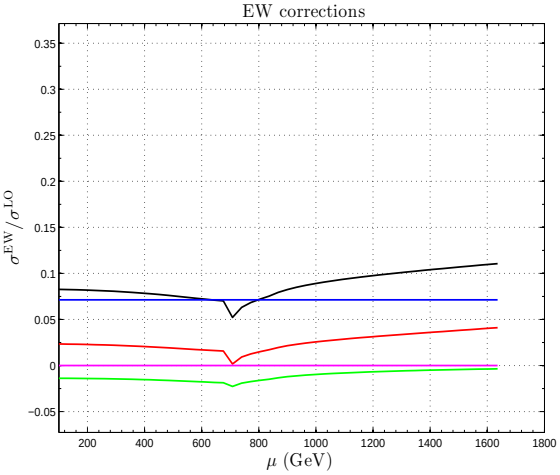

(d)

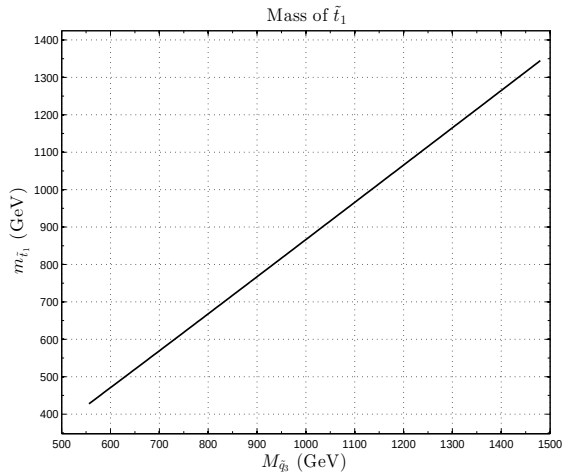

(e)

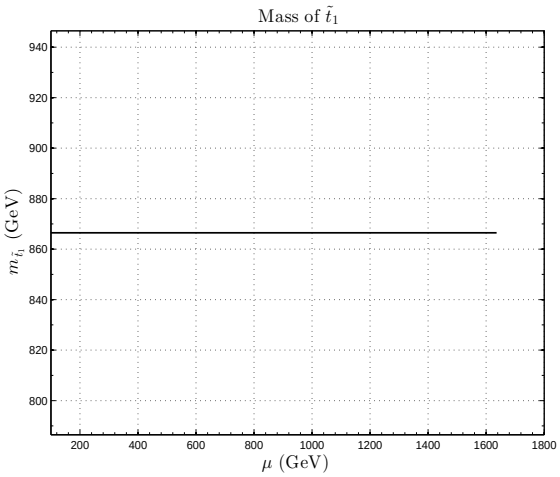

(f)

Figure 5: Same as Fig. 4, but for the light-stau scenario. The value of the parameters not involved in the scans are collected in Table 1(c).

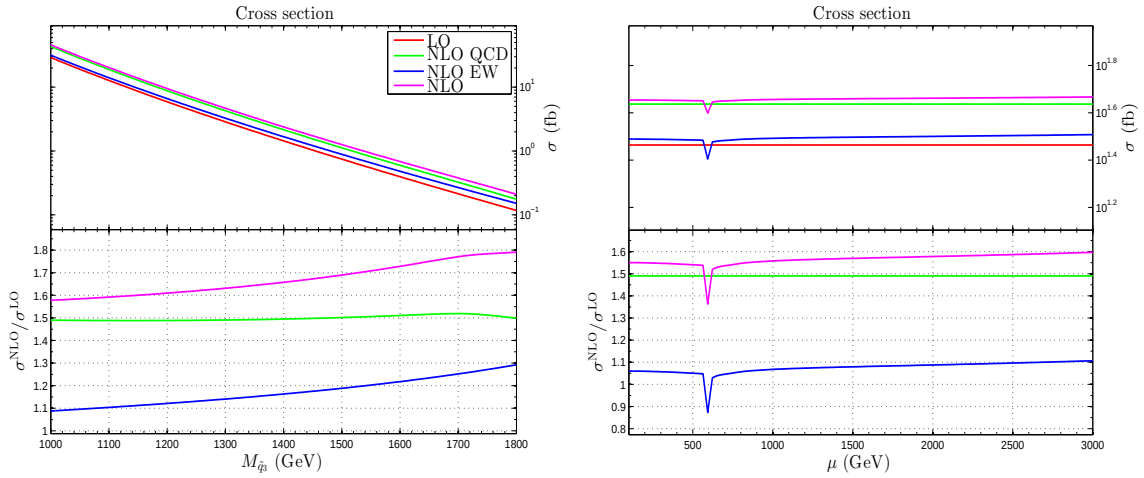

(a)

(b)

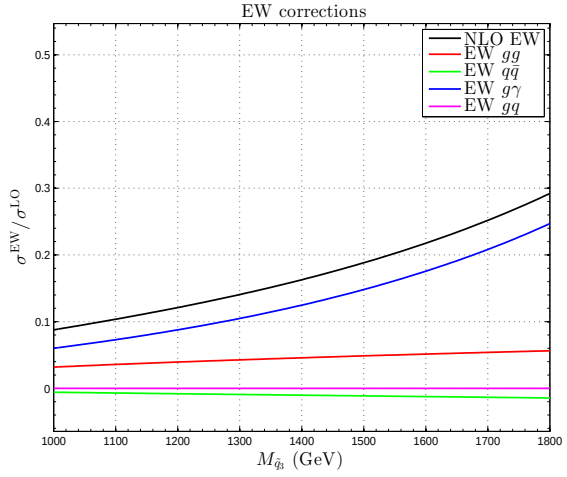

(c)

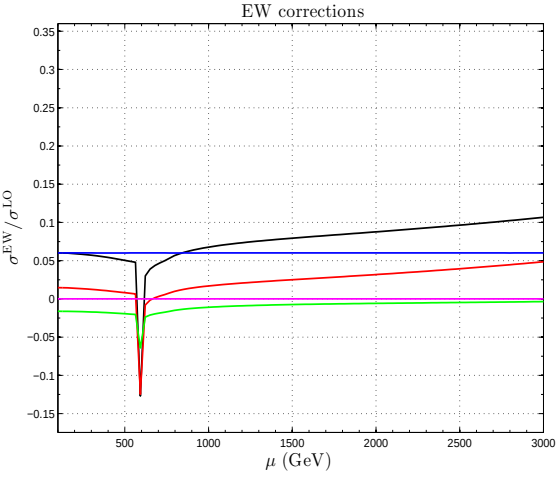

(d)

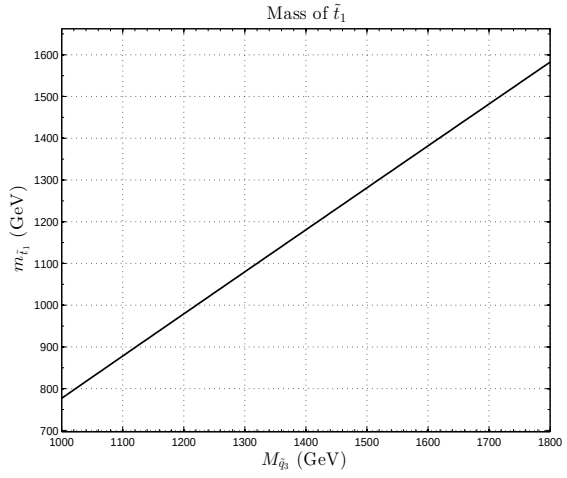

(e)

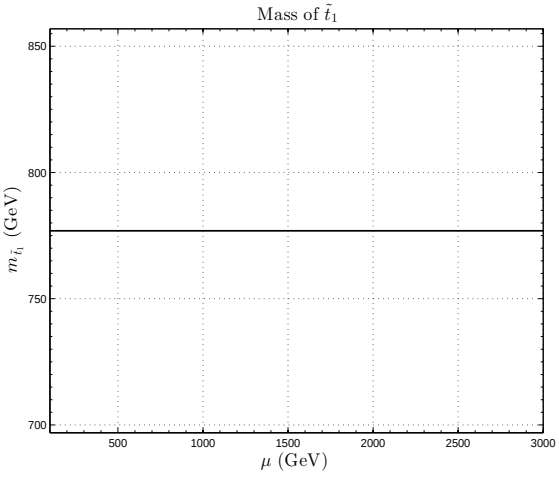

(f)

Figure 6: Same as Fig. 4, but for the tau-phobic scenario. The value of the parameters not involved in the scans are collected in Table 1(d).

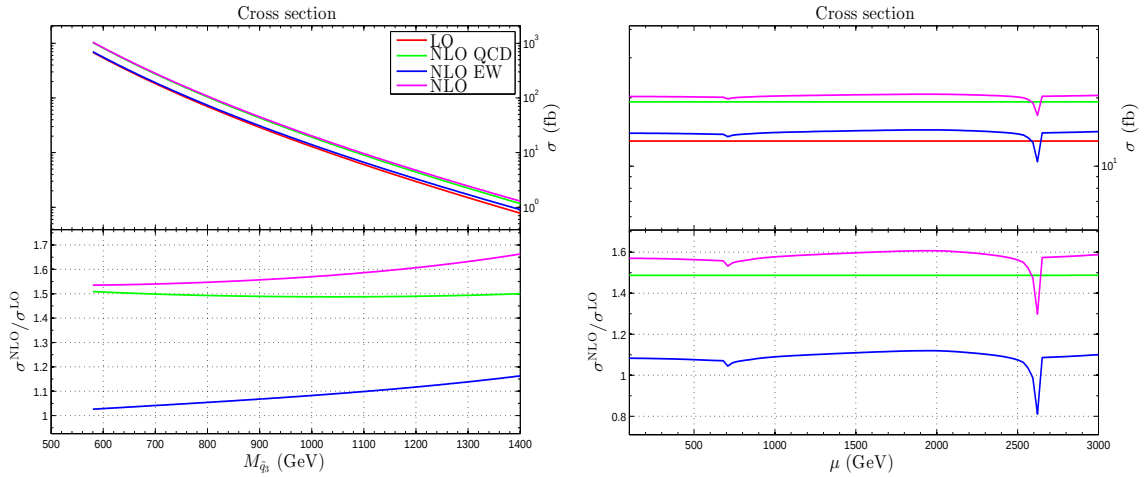

(a)

(b)

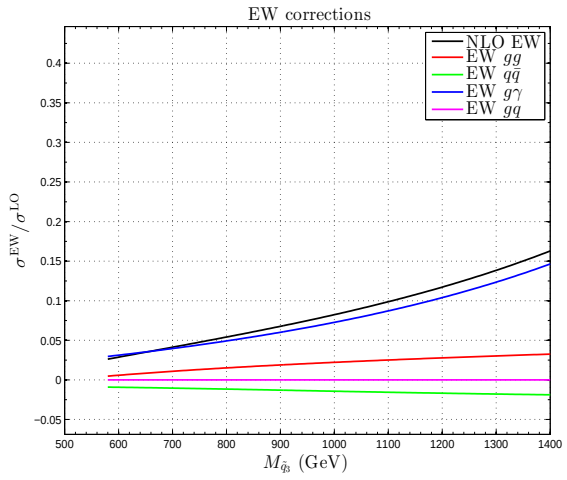

(c)

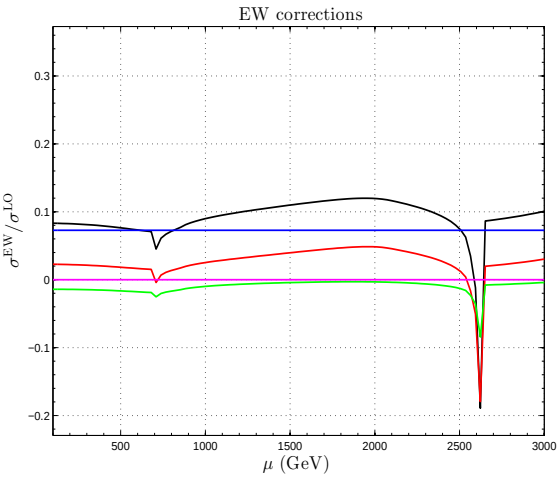

(d)

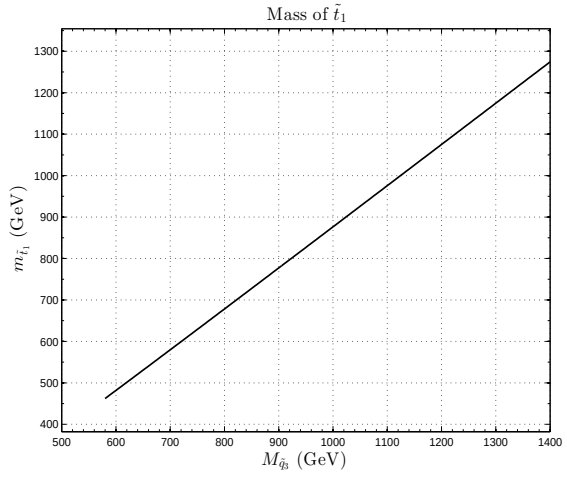

(e)

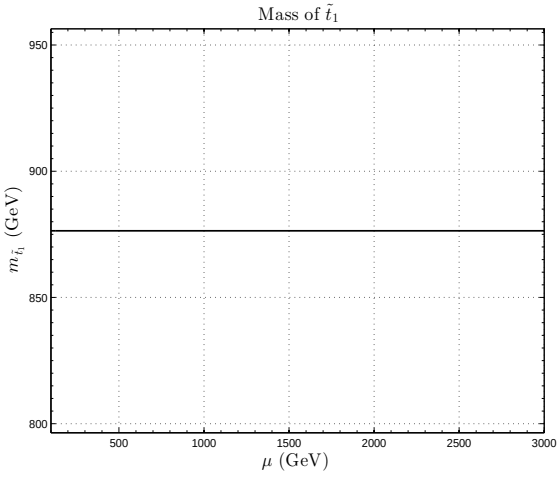

(f)

Figure 7: Same as Fig. 4, but for the $m_h^{\rm mod+}$ scenario. The value of the parameters not involved in the scans are collected in Table 1(e).

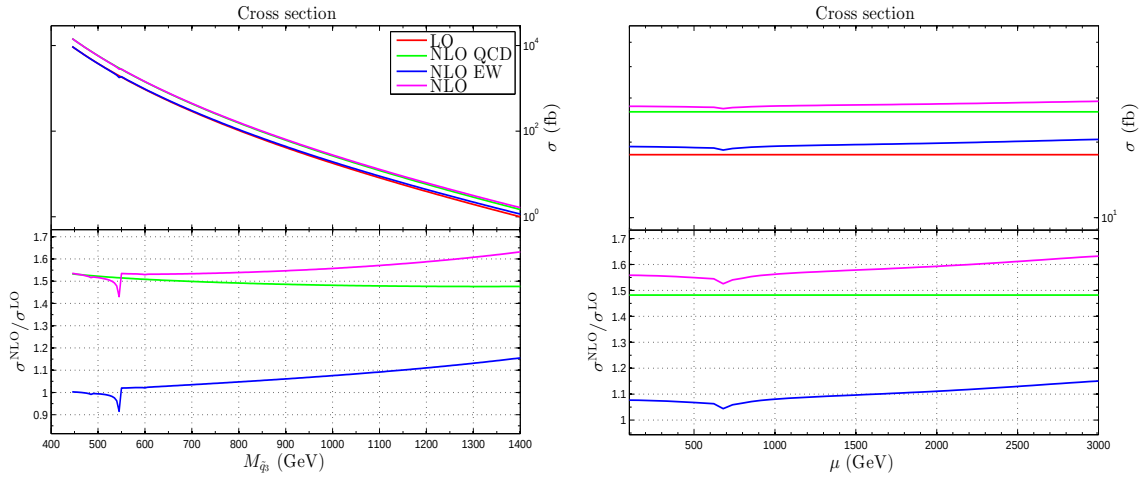

(a)

(b)

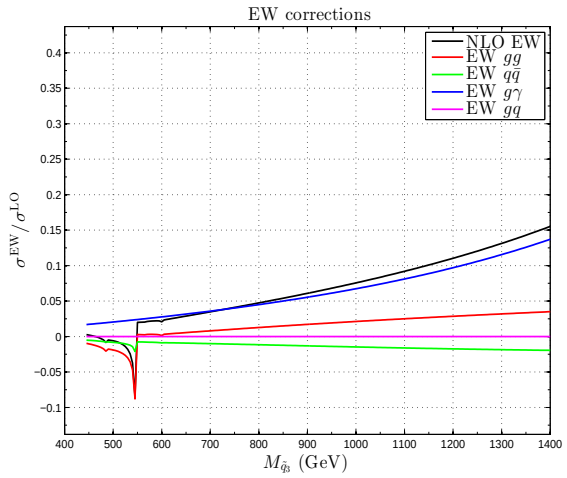

(c)

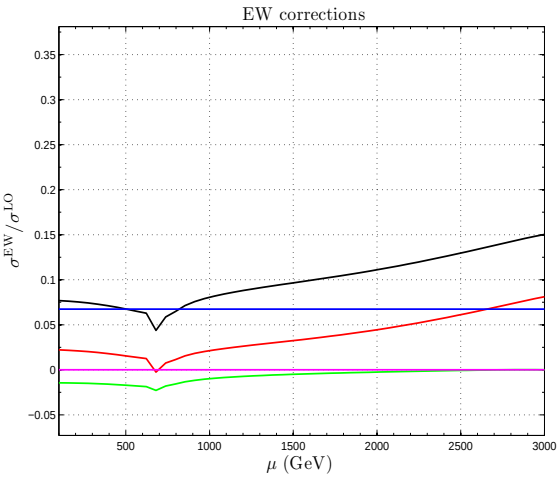

(d)

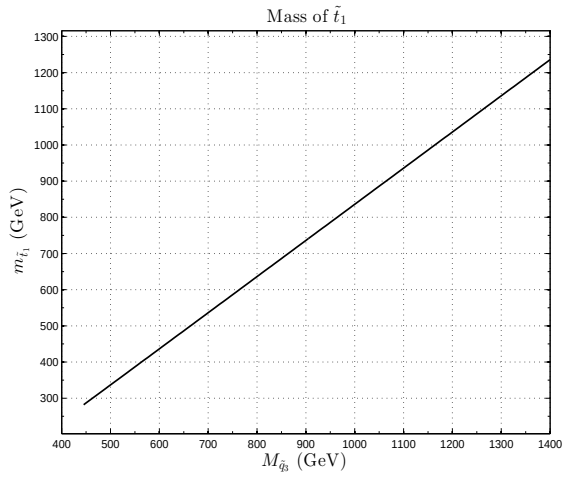

(e)

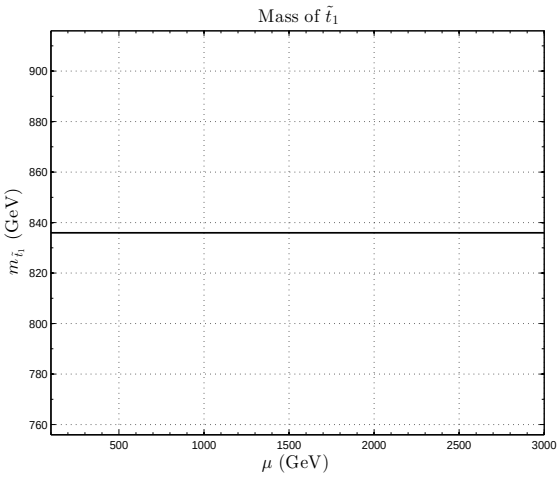

(f)

Figure 8: Same as Fig. 4, but for the $m_h^{\rm mod\,-}$ scenario. The value of the parameters not involved in the scans are collected in Table 1(f).

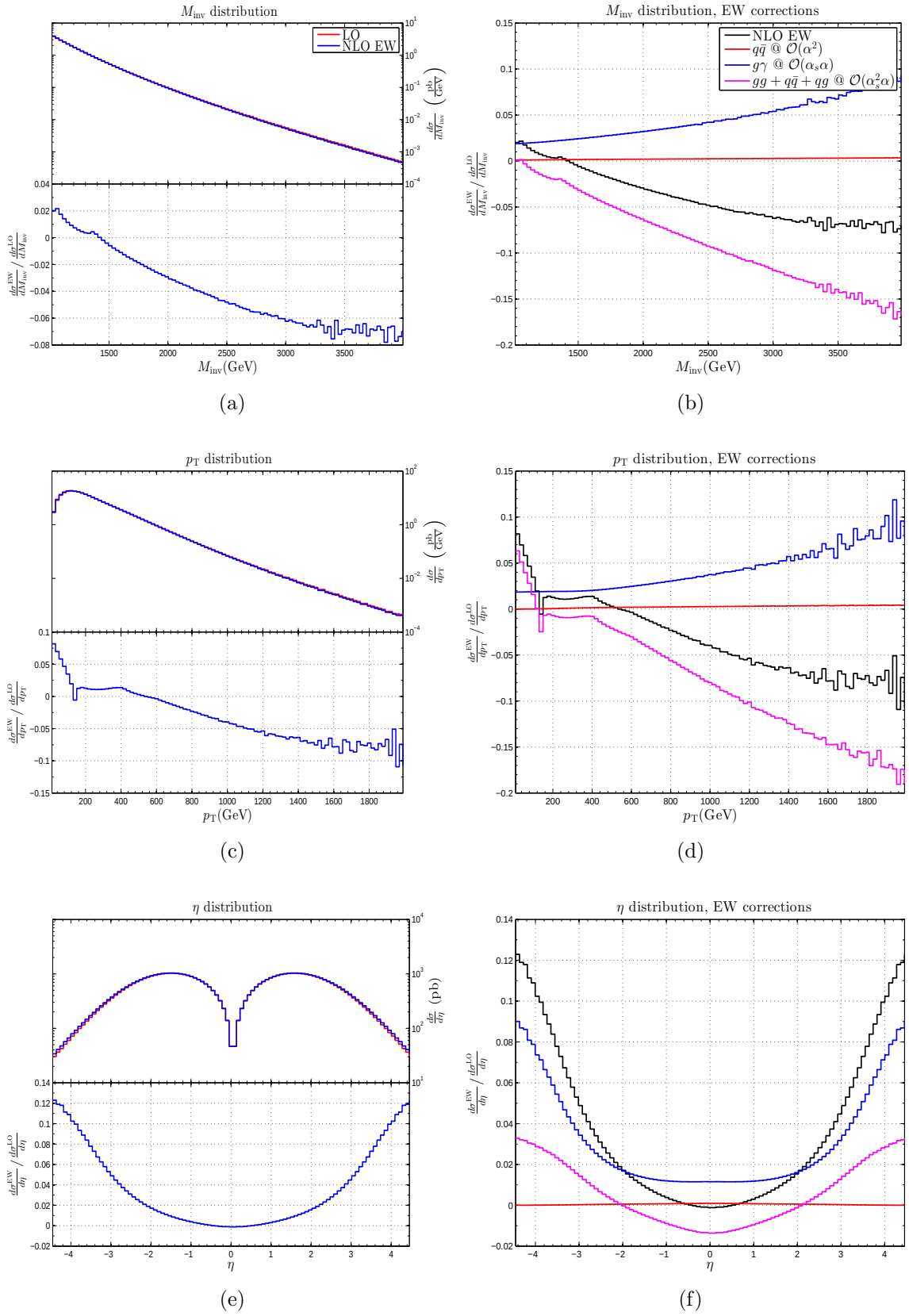

Figure 9: Invariant mass, transverse momentum and pseudo-rapidity distribution in the light-stop scenario defined in Table 1(b).

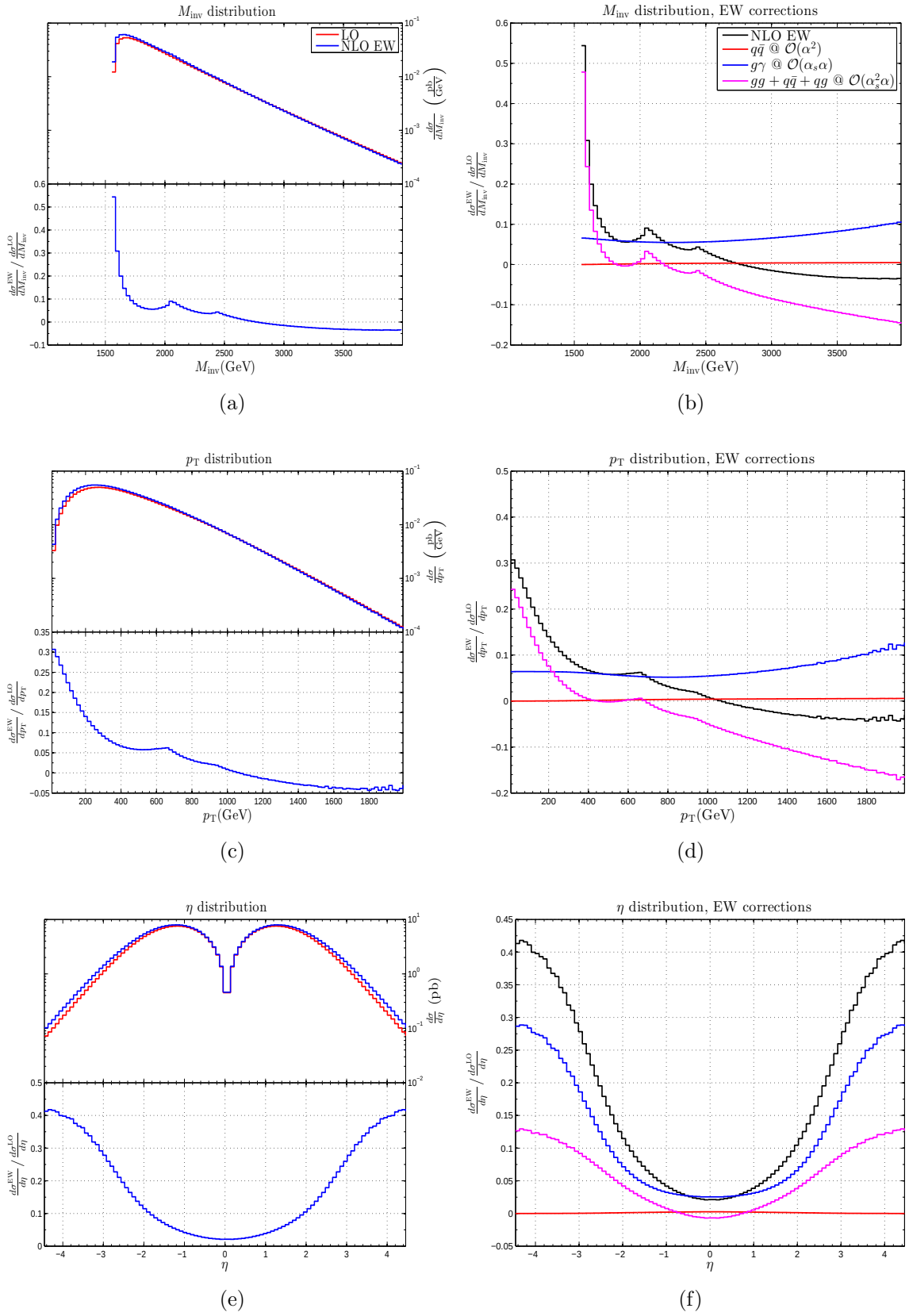

Figure 10: Same as Fig. 9 but for the tau-phobic scenario defined in Table 1(d).